Karlsruhe Institute of Technology

Background investigation for keV-sterile neutrino search with KATRIN

Master thesis
by

Moritz Puritscher

at the Institute for Astroparticle Physics

Reviewer:	Prof. Dr. Guido Drexlin
Second Reviewer:	Prof. Dr. Susanne Mertens
Advisor:	Dr. Dominic Hinz

Bearbeitungszeit: 01.08.2023 – 31.07.2024

Erklärung zur Selbstständigkeit

Ich versichere, dass ich diese Arbeit selbstständig verfasst habe und keine anderen als die angegebenen Quellen und Hilfsmittel benutzt habe, die wörtlich oder inhaltlich übernommenen Stellen als solche kenntlich gemacht und die Satzung des KIT zur Sicherung guter wissenschaftlicher Praxis in der gültigen Fassung vom 24.05.2018 beachtet habe.

Karlsruhe, den 30.07.2024, _____

Moritz Puritscher

Als Prüfungsexemplar genehmigt von

Karlsruhe, den 30.07.2024, _____

Prof. Dr. Guido Drexlin

Contents

1. Introduction

Neutrinos are the second most abundant particle in the universe with a relic neutrino density of 339 $\frac{1}{\mathrm{cm}^3}$[LP12]. Even though they are well-established in the Standard Model (SM) of particle physics there are still several neutrino properties unknown. One of which is the neutrino mass. In the SM neutrinos are assumed to be massless. However, the discovery of neutrino oscillations proves that neutrinos have non-zero mass. Several experiments already determined the mass differences between neutrino states that is required for the neutrino oscillation mechanism. Only the absolute mass scale of neutrinos has not yet been determined, because it is so small.

The KATRIN (**KA**rlsruhe **TRI**tium **N**eutrino) experiment aims to determine the effective neutrino mass with a sensitivity of $< 0.3\,\mathrm{eV}$. This is achieved in a model independent way by studying the kinematic endpoint of tritium β decay electrons. The high-luminosity WGTS (Windowless Gaseous Tritium Source) provides 10^{11} β-electrons per second that are analyzed by a high energy resolution MAC-E filter (Magnetic Adiabatic Collimation with electrostatic filter) type spectrometer. Only electrons above the retarding energy are transmitted onto the detector. By scanning through retarding energies close to the tritium endpoint, KATRIN can search for spectral distortions caused by the effective neutrino mass. Even with an elevated background rate the KATRIN experiment already provides a world-leading upper limit on the neutrino mass of

$$m_\nu < 0.45\mathrm{eV}/c^2 \text{ at } 90\% \text{ C.L.} \tag{1.1}$$

The KATRIN setup can also be used to search for keV-scale sterile neutrinos. Sterile neutrinos are viable dark matter candidates that might also play a role in explaining the smallness of neutrino mass. Through mixing these sterile neutrinos lead to a kink-like signature in the differential tritium β-decay spectrum. In order to differentially measure the tritium spectrum several changes to the beamline have to be made. The retarding energy will be set lower to scan deeper into the β spectrum, while the magnetic field inside the spectrometer has to be increased to ensure adiabatic electron transport. Furthermore, lowering the retarding energy will lead to much higher electron rates on the detector. Therefore, a new high-resolution TRISTAN SDD (Silicon Drift Detector) capable of handling such high rates is developed. Due to the modular design of the TRISTAN SDD, the high outgassing electronics are not fully separated from the ultra high vacuum (UHV) spectrometer section. This can lead to deteriorated vacuum conditions inside the main spectrometer. As counter measure the vacuum system of the detector section will be improved.

Scope of this work is to determine the expected background level for keV-sterile neutrino search at KATRIN. Therefore, the prevailing vacuum conditions inside the main spectrometer for KATRIN operation with TRISTAN modules is determined. Based on previously conducted measurements on the vacuum compatibility of the TRISTAN modules vacuum

simulations are performed using the MolFlow+ software. To improve vacuum compatibility of the detector additional pumps will be implemented on the detector side. Furthermore, a vacuum shield is designed to cover the gaps between modules of the TRISTAN SDD. This prevents a direct line of sight of molecules desorbed from the electronics. With the simulations the impact of additional pumping on the detector side and the effectiveness of the detector vacuum shield can be assessed. Additionally, exploratory background measurements at conditions expected for TRISTAN operation are performed. Most KATRIN backgrounds are related to the large main spectrometer and the background rate dependents on multiple parameters like the electromagnetic settings applied at the spectrometer as well as the pressure, or temperature. When operating KATRIN with TRISTAN modules the retarding energy will be significantly below the tritium endpoint, while the magnetic field in the spectrometer analyzing plane is increased and the vacuum conditions might be deteriorated. For this scenario dedicated background measures are performed and especially the energy distribution of these background electrons is investigated.

Chapter 2 will give an introduction to the history of neutrino physics, their oscillation mechanism and sterile neutrinos. The KATRIN experiment and its setup are described in chapter 3. Background processes related to the KATRIN main spectrometer and the keV-sterile neutrino search with the KATRIN apparatus will also be explained in this chapter. In chapter 4 the vacuum simulations to determine the prevailing pressure in the main spectrometer with an integrated TRISTAN SDD are described. Results of exploratory background measurements at conditions close to the operation with the TRISTAN SDD are presented in chapter 5.

2. Neutrino Physics

Neutrinos are very light electrically neutral fermions that only interact via the weak force. With a density of 339 $\frac{1}{\text{cm}^3}$[LP12] relic neutrinos from the Big Bang are the second most abundable particle in the known universe. Despite their low interaction rate, neutrinos play a vital role in many cosmological phenomena and the evolution of the universe.

Since W. Pauli proposed the existence of such an elusive particle in 1930 [Pau30], the area of neutrino physics has developed to a large and vital research field in particle- and astrophysics. However, it took over 25 years for the first experimental proof of their existence. In 1956, Cowan and Reines [CR$^+$56] where able to observe the imprint of electron neutrinos from a nearby reactor in the Savannah River Experiment. The muon-neutrino was later discovered by Ledermann, Schwartz and Steinberger[LSS$^+$62] in 1962 and only in 2001 the DONUT Collaboration[DON01] was able to observe tau neutrinos. This way completing the fermion doublett structure in the Standard model of particle physics (SM) with all three charged leptons e,μ,τ and their corresponding neutrinos.

Even after the discovery of the three neutrino generations there are still many properties of neutrinos that are to this day unknown. These open questions concerning the absolute mass scale of neutrinos, there Dirac or Majorana nature and the possible existence of sterile neutrinos make Neutrino Physics a very active field.

In this chapter, key experiments for the postulation and discovery of neutrinos are summarized in section 2.1. Section 2.2 gives an introduction to neutrinos as implemented in the Standard model of particle physics. The follwing sections 2.3-2.5 focuses on neutrinos beyond the Standard model. First, neutrino oscillations and their theoretical description is explained in section 2.3, providing proof of non-zero neutrino mass[Pon67]. Afterwards, several approaches to determine the absolute neutrino mass scale are elaborated on in section 2.4. Concluding, section 2.5 explores the well motivated extension of the SM with so-called sterile neutrinos.

2.1. Neutrino Postulation and Discovery

The story of neutrinos starts in 1896 with the discovery of beta rays by Henri Becquerel[Bec96]. Those beta rays consist of electrons, which was shown by Marie and Pierre Curie in 1902[Cur03] and in 1914 J. Chadwick[Cha14] measured the electron energies. In contrast to the other two radioactive processes α and γ decay, these electrons show a continuous energy spectrum. This contradiction to previous observation was puzzling the nuclear physics world. At the time, only protons and electrons have been known as constituents of nuclei. As a consequence the emitted electrons in a two-body decay should have had a discrete energy distribution, since the mass difference between mother and daughter nucleus is almost fully converted into the emitted electrons kinetic energy. While some physicist were thinking about omitting energy conservation, one of the most basic and profound principles in physics, W. Pauli proposed the existence of a new particle. In his famous letter to the Radioactive Society [Pau30] he arguments that the energy conservation principle can be saved, if a very light neutral particle, the neutrino [1] , is emitted along with the electrons. Adding a neutrino to the beta decay products makes it a three-body decay,

$$n \rightarrow p + e^- + \bar{\nu_e} \tag{2.1}$$

so the decay energy - or mass difference between mother and daughter nucleus - is shared between the electron and the neutrino. In each decay the fraction of energy carried away by the neutrino can vary, thereby explaining the observed continuous electron energy spectrum.

Savannah River Experiment
First evidence for the existence of neutrinos was found by C.L. Cowan and F. Reines in 1956 [CR$^+$56]. They detected the signature of inverse beta decay (Equation 2.2) products in a coincidence measurement close to the Savannah River Plant, a nuclear fission reactor

$$p + \bar{\nu_e} \rightarrow n + e^+ \quad . \tag{2.2}$$

Large cadmium doped water tanks served as a proton-rich target for the high anti-neutrino flux coming from the nearby nuclear fission reactor. Positrons produced via inverse beta decay promptly annihilate with electrons emitting two photons with 0.511 MeV in opposite directions. The neutrons on the other hand scatter in the medium until there thermal energy is low enough to be captured by the cadmium atoms. After the neutron is absorbed a gamma ray is emitted with a delay of several microseconds with respect to the prompt positron annihilation. The Savannah river experiment was able to detect these events with a signal-to-noise ratio of 3 using a coincidence study for the specific signatures of positrons and neutrons. Furthermore, they were able to determine the reaction cross section

$$\sigma = 6.3 \cdot 10^{-44} \frac{1}{\mathrm{cm}^2} \quad , \tag{2.3}$$

which is in very good agreement with theoretical predictions. These results present the first direct observations of neutrinos.

Discovery of the muon neutrino
Soon after the discovery of the electron neutrino ν_e, Ledermann, Schwartz and Steinberger found a neutrino ν_μ with different behaviour then ν_e.[LSS$^+$62] They produced a pion beam by focusing high energy protons at the Brookhaven AGS (Alternating Gradient

[1] Pauli actually proposed the name neutron for the postulated particle. This name was thought to be more fitting for the counterpart of the proton, which was discovered in 1932. The particle emitted by beta decay was then renamed to neutrino since it is also electrically neutral, but much lighter than the neutron

Synchrotron) on a Beryllium target. The thereby produced pions decay in flight to produce a neutrino beam.

$$\pi^{\pm} \rightarrow \mu^{\pm} + (\nu_{\mu}/\bar{\nu}_{\mu}) \quad . \tag{2.4}$$

In a distance of 21 m a 13.5 m thick iron shield wall is located to prevent any muons from entering the 10 t aluminum spark chamber detector. In the detector the produced leptons from the reactions

$$\begin{aligned} \nu_{\mu} + n &\rightarrow p + e^{-} \\ \bar{\nu}_{\mu} + p &\rightarrow n + e^{+} \end{aligned} \tag{2.5}$$

$$\begin{aligned} \nu_{\mu} + n &\rightarrow p + \mu^{-} \\ \bar{\nu}_{\mu} + p &\rightarrow n + \mu^{+} \end{aligned} \tag{2.6}$$

are tracked. If the neutrino associated with pion decay would in fact be the same as the neutrino measured from beta decay, the reaction rates for Equation 2.5 and Equation 2.6 have to be the same. During the experiment no electron or positron could be seen in the detector, however there were 29 muon tracks after background cuts. The observed number of muon tracks is furthermore in line with predictions using Fermi interaction. This was prove that the neutrino associated with pion decay is another neutrino than the one associated with beta decay and there are at least two types of neutrinos. After the discovery of the third lepton family, the tauon, in 1975 [P^{+}75] it was only natural to assume the existence of a third neutrino flavor, the tau neutrino ν_{τ}.

Discovery of the tau neutrino
First direct evidence for ν_{τ} was only found in 2001 by the DONUT collaboration[DON01]. A powerful accelerator was needed in order to observe ν_{τ}, due to the large mass of the tauon $m_{\tau} = (1776.93 \pm 0.09)\,\mathrm{MeV}$[N^{+}24] produced in the charged current (CC) reaction

$$\begin{aligned} \nu_{\tau} + n &\rightarrow p + \tau^{-} \\ \bar{\nu}_{\tau} + p &\rightarrow n + \tau^{+} \end{aligned} \quad . \tag{2.7}$$

The Fermilab Tevatron particle accelerator was guiding 800 GeV protons on a tungsten target to create a neutrino beam. The main contribution to ν_{τ} in this neutrino beam was from charmed strange mesons ${D_s}^{\pm}$ decaying to $\tau^{\pm}$-leptons and $\nu_{\tau}/\bar{\nu}_{\tau}$ as well as the following decay of $\tau^{\pm}$ leptons to $\bar{\nu}_{\tau}/\nu_{\tau}$. Same as in the muon neutrino experiment at AGS, the detector was shielded to prevent muons and cosmic rays from entering the detector. In addition to the shielding, several veto systems had been deployed to reject background events. After several quality cuts for recorded neutrino events, a total of 203 events were analyzed and 4 of those events could be identified as τ CC events. This was in line with expectations within a 3σ range and is therefore reported as first direct detection of ν_{τ}.

2.2. Neutrinos in the Standard Model

The standard model is currently the most successful theory in particle physics, describing all known fundamental particles and their interactions via three of the four fundamental forces[2].[N^{+}24] These particles fall into three categories: quarks and leptons (matter particles), gauge bosons (force carriers), and the Higgs boson (see Figure 2.1). Quarks and leptons are fermions with spin-1/2, each having a corresponding antiparticle. Gauge bosons are spin-1 vector bosons and the Higgs is a spin-0 scalar boson.

Matter particles are divided into three generations or flavors of increasing mass. The first generation includes the up and down quark, which are forming protons and neutrons as

[2]Gravity is the only force that can not be described as a quantum field theory in the standard model yet.

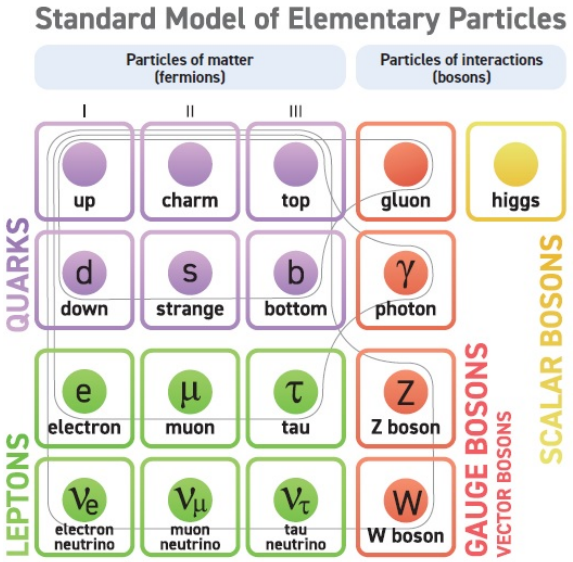

Figure 2.1.: All known particles in the SM. The spin-1/2 fermions on the left hand side can be subdivided into quarks, the constituents of baryons and mesons, and leptons. The spin-1 (or Spin-0 for the Higgs) bosons on the right mediate particle interactions in the SM.[Sha21]

well as the electron and its corresponding neutrino. These first generation quarks and the charged lepton e^- constitute most of the matter. The photon and neutrinos are also abundant. Higher generation particles are unstable, decaying into first-generation particles.

Forces are mediated by gauge bosons, derived from the invariances of the standard model Lagrangian under local gauge transformations. Photons mediate the electromagnetic force between electrically charged particles, gluons mediate the strong force between color charged particles and Z and W bosons mediate the weak force, responsible for phenomena such as beta decay and quark mixing. The electromagnetic and weak forces are unified into the electroweak force. The electroweak interaction is a chiral theory, with particle fields split into left-handed doublets and right-handed singlets of weak isospin. It is spontaneously broken at low energies around $E_c = 159.5\,\text{GeV}$[DR16] via the Higgs mechanism, giving mass to Z^0 and $W^\pm$ bosons. The fourth degree-of-freedom of the Higgs field gives rise to the spinless Higgs boson that was discovered at the Large Hadron Collider (LHC) in 2012[A$^+$12][C$^+$12]. Fermions also acquire there mass through the Higgs field via Yukawa interactions that change the chirality of the interacting fermion.

Neutrinos carry no electrical or color charge, so they are the only fermions that interact solely via the weak force. They also demonstrate parity violation, as shown by the Wu[WAH$^+$57] and Goldhaber[GGS58] experiments, which found that neutrinos are always left-handed and antineutrinos are always right-handed, indicating maximal parity violation in weak interactions. This leads to the assumption that neutrinos need to have zero mass in the SM, because they can not couple to the Higgs field via Yukawa interactions. With the discovery of neutrino oscillations by the Super-Kamiokande[F$^+$98] and the SNO (Sudbury Neutrino Observatory)[A$^+$01] experiment it was revealed that neutrinos have in fact a non-zero mass.

The inclusion of neutrino masses raises several questions. So far, no experiment was able to determine the absolute mass scale of neutrinos, although several upper limits in the eV-range have been established. There is also no proof for any specific mechanism generating the extremely small[3] neutrino masses. Then there is the question about their

[3]Standard model fermion masses already span over 6 orders of magnitude between the lightest particle,

Dirac or Majorana nature. While charged fermions are distinct from there anti-particles by charge conjugation, neutrinos are neutral particles and could be there own anti-particles. Finally, the existence of right-handed, so-called sterile neutrinos is also possible. The name sterile is meant to indicate that they interact only through oscillations and gravity. They could potentially explain the small masses of neutrinos by the seesaw mechanism compared to other fermions and can also be a viable candidate contributing to dark matter.

2.3. Oscillation formalism and mixing parameters

Neutrino oscillations refer to the change of neutrino flavor during their propagation. This transformation of flavor states is only possible if neutrino flavor eigenstates are a superposition of neutrino mass eigenstates implying non-zero neutrino mass. The concept of massive neutrinos and their oscillations was first proposed by Bruno Pontecorvo in 1967[Pon67], spurred by the observed deficit in solar neutrino flux from the Homestake experiment.

In the 1960s, R. Davis and J. Bahcall designed and built an experiment aimed at detecting neutrinos from the sun's nuclear fusion processes.[DHH68] Based on the Standard Solar Model (SSM), the expected solar neutrino spectrum as shown in Figure 2.2 is well-defined.[BBS68, BU88, BSB05]

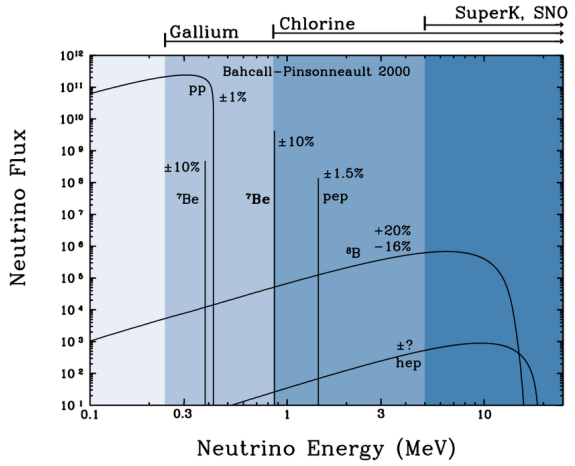

Figure 2.2.: Neutrino flux predicted by the SSM. The fluxes are split into main nuclear reactions of their production meachanism in the sun. At the top of the figure are the thresholds for different solar neutrino experiments indicating their sensitivity to neutrino production mechanism in the sun.[Bel04]

The experiment, located in the Homestake Gold Mine in South Dakota, used a 390'000-liter tank of tetrachloroethylene to capture neutrinos via inverse beta decay:

$$\nu_e + {}^{37}\mathrm{Cl} \rightarrow {}^{37}\mathrm{Ar} + e^- \quad . \tag{2.8}$$

Despite the theoretical prediction of a capture rate of 7.6 SNU[4] (solar neutrino units), the measured rate was only 2.56 SNU, about a third of the expected value. This discrepancy, known as the solar neutrino problem, was later confirmed by several other experiments. Especially the results from the Kamiokande-II water cherenkov detector supported the Homestake findings, because they were additionally able to pinpoint the neutrino flux direction back to the sun[Suz91]. Neutrino Oscillation theory provided the most promising solution toward the solar neutrino problem.

the electron, and the heaviest particle, the top quark. However, the neutrino mass is again at least 5 orders of magnitude smaller than the electron.

[4] 1 SNU corresponds to 1 reaction per second per 10^{36} atoms in the detector

The first concrete evidence of neutrino oscillations came from the Super-Kamiokande experiment [F$^+$98], which detected a deficit of atmospheric muon neutrinos inconsistent with theoretical predictions. This discrepancy was later investigated by the SNO experiment [A$^+$01], which measured the flux of electron neutrinos separately from the total neutrino flux. Their results showed that the total neutrino flux matched the predictions of the SSM, while the flux of electron neutrinos alone was significantly lower, thereby confirming neutrino oscillations at 90% confidence level.

Neutrino Oscillation Theory

The theory of neutrino oscillations is analogous to quark mixing, where the eigenstates of the weak interaction (flavor eigenstates) are not the same as the mass eigenstates. For neutrinos, the flavor eigenstates ν_e, ν_μ, ν_τ are superpositions of the mass eigenstates ν_1, ν_2, ν_3. This relationship is described by the Pontecorvo-Maki-Nakagawa-Sakata (PMNS) matrix U:

$$|\nu_\alpha\rangle = \sum_{j=1}^{3} U_{\alpha j} |\nu_j\rangle \tag{2.9}$$

with α representing the flavor state e,μ,τ and j the mass state 1,2,3.[N$^+$24] The PMNS matrix U is a 3×3 unitary matrix that can be parameterized by three mixing angles θ_{12}, θ_{23}, θ_{13} and one CP-violating phase

$$U_{\text{PMNS}}^{(\text{D})} = \begin{pmatrix} U_{e1} & U_{e2} & U_{e3} \\ U_{\mu 1} & U_{\mu 2} & U_{\mu 3} \\ U_{\tau 1} & U_{\tau 2} & U_{\tau 3} \end{pmatrix} = \begin{pmatrix} 1 & 0 & 0 \\ 0 & c_{23} & s_{23} \\ 0 & -s_{23} & c_{23} \end{pmatrix} \begin{pmatrix} c_{13} & 0 & s_{13}e^{-i\delta} \\ 0 & 1 & 0 \\ -s_{13}e^{i\delta} & 0 & c_{13} \end{pmatrix} \begin{pmatrix} c_{12} & s_{12} & 0 \\ -s_{12} & c_{12} & 0 \\ 0 & 0 & 1 \end{pmatrix} \tag{2.10}$$

Here, $c_{ik} = \cos\theta_{ik}$ and $s_{ik} = \sin\theta_{ik}$. The phase δ indicates CP-violation in neutrino oscillations if it is non-zero. For the case of neutrinos being Majorana particles two additional phases β_1 and β_2 are added with respect to the Dirac PMNS matrix $U_{\text{PMNS}}^{(\text{D})}$

$$U_{\text{PMNS}}^{(\text{M})} = U_{\text{PMNS}}^{(\text{D})} \begin{pmatrix} e^{i\beta_1/2} & 0 & 0 \\ 0 & e^{i\beta_2/2} & 0 \\ 0 & 0 & 1 \end{pmatrix} \tag{2.11}$$

A large number of experiments is determining the mixing angles and mass splittings between neutrino states.[A$^+$22a, A$^+$23a, A$^+$23b, A$^+$23c] Several different neutrino sources can be utilized to observe neutrino oscillations, there are solar, atmospheric and reactor neutrinos and also neutrino beams produced in particle accelerators. Most of these experiments can effectively reduce the neutrino oscillation to a 2-flavor mixing, simplifying the evaluation with respect to the mixing parameters. The probability for a produced neutrino of flavor α to be measured as a neutrino of flavor β for two flavor neutrino mixing is given by

$$P(\nu_\alpha \to \nu_\beta) = |\langle \nu_\beta | \nu_\alpha(t) \rangle|^2 = \sin^2(2\theta)\, \sin^2\left(\frac{1.27 \cdot \Delta m_{jk}^2[\text{eV}^2] \cdot L[\text{km}]}{4E[\text{GeV}]} \right) \tag{2.12}$$

Here, $\theta_i k$ is the neutrino mixing angle, $\Delta m_{ik}^2 = m_i^2 - m_k^2$ is the mass splitting, L is the distance between the source and detector and E is the neutrino's energy. This expression shows that neutrino oscillations depend on the mass differences and the mixing angles. It

Table 2.1.: Experimental results summarized by the particle data group[N$^+$24] for all mixing parameters and the experimental type that is mainly sensitive to this parameter

mixing parameter	best-fit value	sensitive experiments
Δm^2_{21}	$(7.53 \pm 0.18)\,\mathrm{eV}^2$	solar experiments
Δm^2_{32}	$(2.455 \pm 0.028)\,\mathrm{eV}^2$	atmospheric and LBL accelerator experiments
$\sin^2\theta_{12}$	(0.307 ± 0.013)	solar Experiments
$\sin^2\theta_{23}$	(0.558 ± 0.015)	atmospheric and LBL accelerator experiments
$\sin^2\theta_{13}$	(0.0219 ± 0.0007)	reactor experiments
δ_{CP}	(1.19 ± 0.22)	LBL accelerator experiments

also shows that all above mentioned neutrino sources can be used to investigate specific L/E ratios in different experiments.

The most recent results for the individual mixing parameters, neglecting the Majorana phases are summarized in Table 2.1. Listed in this table is also the dominant experimental type contributing to the measurements of individual parameters.

2.4. Neutrino Mass Measurements

Ever since the observation of neutrino oscillations has proven the neutrino mass to be non-zero, efforts to determine the absolute neutrino mass scale are intensifying. So far, no determination of the neutrino mass scale was possible, because it is so small. However, knowledge about the neutrino mass scale would provide valuable constraints on beyond SM theories and on the other hand it is also a crucial parameter to understand the evolution of the early universe. There are currently 3 different approaches to determine the neutrino mass scale, each offering some advantages and draw backs[DHMW13].

Cosmological Constraints

Although the mass of neutrinos is so small, they have a great impact on the evolution of the universe. Todays structure is the consequence of small fluctuations in the early stages of the universe. With there small mass and high abundance of 339 relic neutrinos per square centimeter[LP12] from the big bang, neutrinos act as hot dark matter smearing out those fluctuations on small scales. The scale on which these interactions happen is determined by the neutrinos free streaming length that mainly depends on their mass.[BES80][LP06] Observing the distribution of galaxies in large scale galaxy observations like the SDSS (Sloan Digital Sky Survey) and fluctuations of the CMB (Cosmic Microwave Background) one can infer limits on the sum of the neutrino masses.[BMT04] Determination of cosmological limits is however always model dependent.

Neutrinoless Double Beta Decay

Neutrinoless double beta decay ($0\nu\beta\beta$) is a hypothetical decay process in which a nucleus emits two beta electrons simultaneously without accompanying neutrinos. This process is possible if neutrinos are Majorana fermions, meaning they are their own antiparticles. The decay rate of this process is proportional to the square of the effective electron neutrino Majorana mass m_{ee}

$$\Gamma_{0\nu\beta\beta} \propto m^2_{ee} = \left| \sum_{i=1}^{3} U^2_{ei} m_i \right|^2 \text{ [DHMW13]} \tag{2.13}$$

This mass is a coherent sum of all neutrino masses weighted by the PMNS matrix elements. Neutrinoless double beta decay experiments, such as MAJORANA[A$^+$21b], GERDA[A$^+$20a]

and there successor LEGEND[Cal24], aim to detect this rare process. These experiments use the isotope ^{76}Ge. There are several other isotopes suitable for $0\nu\beta\beta$ decay searches[DPR19] for example ^{136}Xe used in the EXO experiment[K$^+$23] or ^{128}Te/^{130}Te in the CUORE experiment[A$^+$22b, A$^+$22c]. To date, no conclusive evidence of $0\nu\beta\beta$ has been observed. Only lower limits on the lifetime in the order of 10^{23}yr have been established.[N$^+$24]

Direct Kinematic Measurements

Direct kinematic measurements offer the most model-independent method for determining the neutrino mass, relying on the relationship $E^2 = p^2 + m^2$. This technique measures the kinetic energy of electrons from beta decay, enabling the determination of the neutrino mass scale.

In a single beta decay, a neutron converts into a proton, an electron, and an electron antineutrino:

$$^A_Z X \rightarrow ^A_{Z+1} Y + e^- + \bar{\nu}_e \tag{2.14}$$

The electron's kinematics contain information about the neutrino mass, most noticeably near the endpoint energy E_0, where the decay energy is maximally transferred to the electron and the neutrino has minimal momentum. Past measurements with experiments in Mainz and Troitsk set an upper limit on the neutrino mass of $m_\nu < 2\,\text{eV}$. The KATRIN experiment already improved upon these limits after the first measurement campaign[A$^+$19a]. Evaluation of the first 5 measurement campaigns further improves the upper limit on the neutrino mass to $m_\nu < 0.45\,\text{eV}$[A$^+$24]. Utilizing a complex and dedicated setup, KATRIN represents a significant advancement in the direct measurement of the absolute neutrino mass scale.

2.5. Sterile Neutrinos

Neutrinos are the only particles in the standard model that have only been observed in states of left-handed chirality. So introducing right-handed neutrinos into the standard model presents a well motivated extension of the SM. These sterile neutrinos naturally provide neutrino masses through the Higgs mechanism. In some theories they can also explain the smallness of the active neutrino masses via the see-saw mechanism. As singlets under the SM gauge group they do not interact via the SM forces, which is why they are often referred to as sterile neutrinos. They can however interact gravitationally and they can mix with the left-handed or active neutrinos through the neutrino oscillation framework. There are only little theoretical and experimental limitations to the number of sterile neutrinos, their mass and their Dirac or Majorana nature. [Vol02]

Depending on their mass scale sterile neutrinos can account for different experimental and cosmological phenomena. Sterile neutrino masses in the order of several eV can pose a compelling solution to the measured anomalies observed at different experiments. The $\nu_e/\bar{\nu}_e$ appearance experiments LSND[AAB$^+$01] and MiniBooNE[AA$^+$18] observed an excess of electron(positron)-like events. This excess can be explained by introducing a 4th neutrino with a mass in the eV scale. The introduction of such a sterile neutrino can also explain the measured deficit in the Gallium radioactive source experiments[GL11][KSGS19] as well as short baseline reactor experiments like Double Chooz.[GL11] However, there are tensions between the data from appearance and disappearance experiments for combined fits under the assumption of one ore more additional sterile neutrinos, with a compatibility below 0.2%.[KMMS13]

A very promising model beyond the standard model is the neutrino minimal standard model (νMSM)[Sha07][BRS09]. It can explain a multitude of experimental and cosmological

observations. For the νMSM three sterile neutrinos are introduced to the SM. Two of those have a mass in the range of hundreds of MeV to the electroweak scale and the third one has a mass on the keV scale.

The mass range of the two heavy sterile neutrino present a promising explanation for the small active neutrino masses via the low scale seesaw mechanism. In that case active neutrino masses are approximately proportional to the inverse sterile mass.[DGGK17] They can also explain the observed baryon asymmetry in the universe by leptogenesis from neutrino oscillations.[CS10]

The neutrino in the keV range can act as a dark matter candidate. Depending on the production mechanism in the early universe keV-sterile neutrinos can either act as warm dark matter (WDM)[DW94] or cold dark matter (CDM)[SF99]. They are neutral, massive and only interact with SM particles through oscillation into the active neutrino states. As massive particle with coupling to lighter SM particles keV-sterile neutrinos are also unstable.[PW82] They can decay into an active neutrino under the emission of X-rays[WLP12]. They still propose a viable dark matter candidate if their lifetime, that is governed by their mixing angle[BDL$^+$19], is longer than the age of the universe.

It is possible to search for sterile neutrinos in the keV range with laboratory experiments. Sterile neutrinos would lead to a distinct kink-like distortion in the tritium β-decay spectrum that can be observed with the KATRIN experiment (see section 3.3).

3. The KATRIN Experiment

The **KA**rlsruher **TR**itium **N**eutrino Experiment (KATRIN) measures the neutrino mass in a model-independent way, by observing the kinematic endpoint of the tritium β-spectrum. Due to the high activity molecular tritium source and the high resolution MAC-E filter type spectrometer, KATRIN aims to determine the neutrino mass with a sensitivity of $< 0.3\,\mathrm{eV}$ (90% CL)[Peh24] after 1000 days of data taking. Thereby, improving on previous neutrino mass limits set by its predecessor experiments, the Mainz[K$^+$04] and Troitsk[A$^+$11] neutrino experiment, by almost an order of magnitude. In order to reach such a high sensitivity, an advanced setup with well developed monitoring systems and elaborate background reduction methods are needed.

The measurement apparatus of the KATRIN experiment is described in section 3.1. Contribution from background electrons that are produced in the spectrometer section of the experiment will be described in section 3.2, as well as implemented mitigation techniques for the described background electrons. The β-decay electrons of the KATRIN source also allow for the search of keV-scale sterile neutrinos. To utilize the KATRIN hardware a new Silicon Drift Detector (SDD) is developed for the TRISTAN (**TR**itium **I**nvestigation on **ST**erile to **A**ctive **N**eutrino mixing) project. The design and integration of this new TRISTAN SDD into the KATRIN beamline will be discussed in section 3.3. With this new high resolution detector, a deeper look into the β-spectrum is possible with a differential measurement of the β-electrons.

3.1. Experimental setup of the KATRIN experiment

The KATRIN experiment aims to determine the absolute mass scale of the electron antineutrino in a direct and model-independent way by studying the kinematics of tritium β-decay. A gaseous molecular tritium source is selected for its low endpoint energy $E_0 \approx 18.6\,\text{keV}$ and relatively short half-life $t_{1/2} = 12.32\,\text{yr}$. To achieve the high sensitivity goal, a very stable source with high luminosity is required, along with a high energy resolution device, provided by a spectrometer operated as a Magnetic Adiabatic Collimation with Electrostatic (MAC-E) filter.

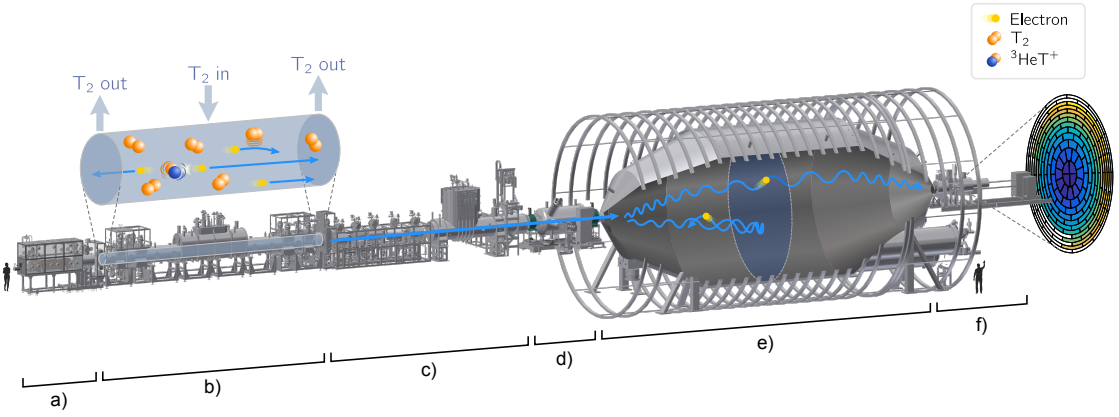

Figure 3.1.: Overview of the 70 m long KATRIN beamline. Tritium gas is injected into the center of the WGTS (b) where it decays and emits electrons. These β electrons are then guided through the transport section (c), consisting of the DPS and CPS. They are then passing through the high pass filter of the Pre- (d) and Main Spectrometer operated as MAC-E filters. Only electrons close to the tritium endpoint can reach the detector (f). (a) shows the rear wall section which includes calibration sources and monitoring devices.

A sketch of the approximately 70 m long setup is depicted in Figure 3.1. The tritium gas is injected into the windowless gaseous tritium source (WGTS) and decays inside the beam tube, emitting β-electrons. These electrons are then adiabatically guided towards the spectrometer by superconducting solenoids around the beam tube. While the electrons are guided through the differential and cryogenic pumping sections (DPS and CPS), the flow of tritium and ions into the spectrometer is reduced by 14 orders of magnitude, preventing contamination of the spectrometer. In the spectrometer, electrons are separated by applying a high-pass filter qU_{ret}. All electrons with a kinetic energy below the retarding energy are reflected at the analyzing plane, shown as the lower electron track in figure 3.1. Only electrons with an energy above this retarding energy are transmitted through the main spectrometer (upper electron track in figure 3.1) and can reach the focal plane detector (FPD). There they are counted on the pixelated silicon p-i-n FPD, measuring the integral electron rate. Scanning of the endpoint region is achieved by varying the retarding energy applied to the main spectrometer.

All the sub-components of the KATRIN experimental setup will be further explained in the following sections. Unless specified otherwise, the information in this chapter is based on the design reports and first measurement result publications [A$^+$05, A$^+$21a, A$^+$19a, A$^+$22d].

3.1.1. Source and transport section

The starting point of the measured electrons is inside the WGTS (Figure 3.1 b), a 10 m long stainless steel beam tube with a 9 cm diameter. High-purity molecular tritium gas is injected into the center of the beam tube and diffuses towards the ends of the WGTS. At

both ends of the WGTS the tritium gas is continuously pumped out by 6 turbomolecular pumps on each side. To reduce the amount of tritium that has to be injected, the beam tube is cooled down to 30 K by a custom designed two-phase neon cooling system. This also reduces any effect of thermal Doppler broadening on the measured electron spectra.

Deploying such a mode of operation, also ensures a constant level of tritium can be maintained inside the WGTS, expressed by the column density of $\rho d \approx 5.0 \cdot 10^{17}$ molecules/cm^2. The electrons generated in the source are adiabatically guided towards the spectrometers by the afforementioned solenoids. On their way through the transport section (Figure 3.1 c), they pass through two chicanes, where the tritium flow is drastically reduced, ensuring no tritium enters the spectrometer section. This is achieved by the Differential Pumping Section (DPS) and the Cryogenic Pumping Section (CPS), which reduce the tritium flow by 14 orders of magnitude.

Within the DPS, β-electrons are guided through a strong magnetic field of 4.0 T, overcoming four bends of 20° each. Turbo molecular pumps installed on these bends reduce tritium flow with an increased effective pumping rate by 7 orders of magnitude. Other molecules are efficiently removed from the beam tube as well, preventing them from flowing straight to the spectrometers. The Cryogenic Pumping Section additionally includes a liquid-helium-cooled 3 K inner surface, covered by an adsorbed argon frost layer. This argon frost cryosorbs any tritiated molecules, reducing the tritium flow by another 7 orders of magnitude.

3.1.2. Spectrometer and detector section

Both the Pre-Spectrometer (PS) and the Main Spectrometer (MS) are operated as MAC-E (Magnetic Adiabatic Collimation with Electrostatic) filters. It serves as a high-pass filter for the β-electrons from the source. A static retarding potential below the endpoint can be applied at the PS to strongly reduce the flux of β electrons into the MS.

The electrons are generated isotropically in the source. As a consequence, their momentum vector has a polar angle θ relative to the magnetic field lines. This leads to a cyclotron motion of the electrons around the magnetic field lines, because of the radial Lorentz force. The total momentum of electrons can therefore be split into a parallel and transverse component of momentum. The filtering electric field only affects the longitudinal component. To achieve a good energy resolution, it is necessary to transform the transverse momentum component $E_\perp$ into the longitudinal one $E_\parallel$. This is achieved by lowering the magnetic field several orders of magnitude from the entrance of the spectrometer to the so-called analyzing plane, where the maximum retarding potential $-U_{\mathrm{max}}$ and minimal magnetic field B_{min} are located (see dashed green line in Figure 3.2). The magnetic moment $\mu = \frac{E_\perp}{B}$ of the electrons cyclotron motion is conserved and the energy resolution is given by the remaining transverse momentum

$$\Delta E = \frac{B_{\mathrm{min}}}{B_{\mathrm{max}}} \cdot E_{\mathrm{kin}} \quad , \tag{3.1}$$

For the design values of $B_{\mathrm{min}} = 3 \cdot 10^{-4}$ T and $B_{\mathrm{max}} = 6$ T KATRIN reaches an unprecedented energy resolution of $\Delta E \approx 1$ eV for endpoint electrons with $E_{\mathrm{kin}} = 18.6$ keV

The main spectrometer's dimensions are established by the conservation of the magnetic flux $\Phi \propto A \times B$. Since the magnetic field drops by four orders of magnitude to the analyzing plane, the area of the flux tube must increase accordingly. Consequently, the main spectrometer was built with a length of 23.8 m and a diameter of 9.8 m. The entire spectrometer is set to high voltage, which is changed in steps of $\Delta U \approx 0.5$ V to 1 V to record the integral spectrum. Additionally, it is equipped with an inner electrode system that has a higher voltage than the vessel, shielding secondary electrons from the wall to prevent background production.

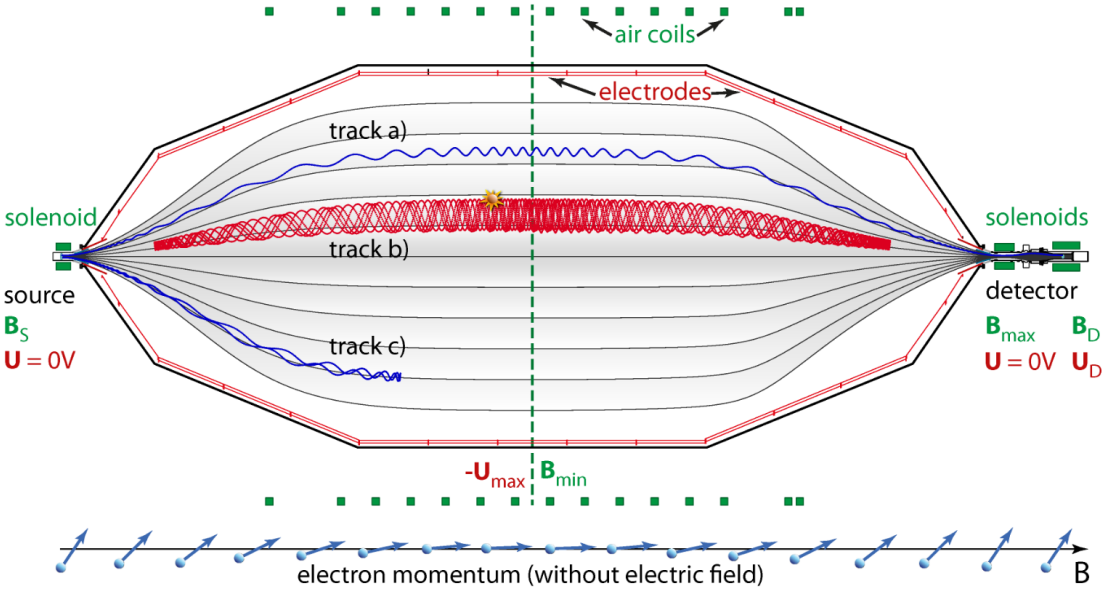

Figure 3.2.: The MAC-E filter principle. The three electron tracks shown correspond to a β electron passing (track a) or being rejected by (track c) the high pass filter. Track b) shows a background electron being trapped due to the magnetic bottle effect. The yellow star indicates the production point for the magnetically trapped background electron.

To prevent residual gas scattering of the β-electrons, both spectrometers are operated under Ultra High Vacuum (UHV) conditions of about 10^{-11} mbar, guaranteed by several getter and turbo molecular pumps (TMP). Large coils surround the spectrometer to prevent the influence of the Earth's magnetic field and allow fine-tuning of the magnetic field at the analyzing plane, by the Earth Magnetic Field Compensation System (EMCS) and the Low Field Compensation System (LFCS).

After passing through the spectrometer, the magnetic flux tube size is reduced by the pinch magnet and the electrons are guided onto the detector by the detector magnet. The Focal Plane Detector (FPD) counts the electrons using a silicon PIN-diode array with high efficiency and minimal background. It is divided into 148 pixels arranged in 12 concentric rings, which are azimuthally subdivided into 12 pixels plus 4 center pixels. The electrons pass the analyzing plane at different radii, experiencing slightly different potentials due to inhomogeneities. This arrangement provides spatial resolution and detects irregularities in the retarding potential.

3.1.3. Neutrino mass determination with KATRIN

The KATRIN experiment extends the work of the Mainz and Troitsk experiments, employing a similar approach to independently measure the mass of the electron neutrino. These experiments study the kinematics of electrons emitted during the beta decay of tritium (T_2) near the energy endpoint:

$$T_2 \rightarrow THe^+ + e^- + \bar{\nu}_e \tag{3.2}$$

The decay rate near the endpoint, assuming a single neutrino mass eigenstate m_ν, is given by:

$$\frac{dN}{dE} = C \cdot F(E,Z) \cdot p \cdot (E + m_e) \cdot (E_0 - E) \cdot \sqrt{(E_0 - E)^2 - m_\nu^2}, \tag{3.3}$$

where E is the electron energy, p its momentum, and m_e its mass. E_0 is the endpoint energy, which is 18.6 keV for a massless neutrino ($m_\nu = 0$). The Fermi function $F(E, Z)$ accounts for Coulomb interactions between the electron and daughter nucleus, and the constant $C = \frac{G_F^2}{(2\pi)^3} \cdot \cos^2\theta_C \cdot |M|^2$ comprises the Fermi constant G_F, the Cabibbo angle θ_C, and the nuclear transition matrix element M. For tritium decay, the transition is super-allowed due to a common ground state between T and He^+, leading to an energy-independent transition matrix M.

In reality, there are multiple neutrino mass eigenstates $m(\nu_i)$, so the observed spectrum is a superposition of spectra for each eigenstate, weighted by their mixing amplitude U_{ei}:

$$\frac{dN}{dE} = C \cdot F(E,Z) \cdot p \cdot (E + m_e) \cdot (E_0 - E) \sum_i |U_{ei}|^2 \cdot \sqrt{(E_0 - E)^2 - m(\nu_i)^2}. \tag{3.4}$$

Due to the small mass splittings between the eigenstates, an effective neutrino mass $m^2_{\text{eff}} = \sum_{i=1}^{3} |U_{ei}|^2 m(\nu_i)^2$ is introduced, which is the observable in the KATRIN analysis.

The integral β-decay spectrum is measured at several retarding energy settings qU_i close to the tritium endpoint energy $E_0 = 18.574\,\text{eV}$. The measurement time distribution (MTD) at each retarding energy setting is optimized with respect to maximal neutrino mass sensitivity.

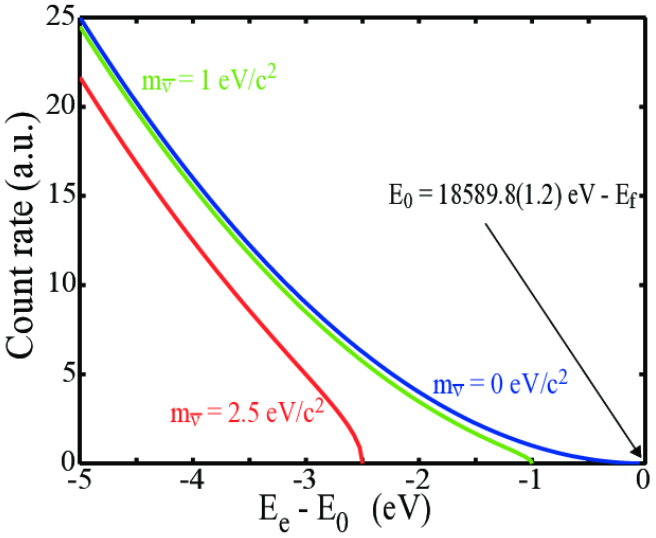

Figure 3.3.: Impact of neutrino mass on the endpoint of the tritium β decay spectrum. The different colored lines show the distortion of the spectral shape for different neutrino masses.[Die11]

To infer the neutrino mass, the spectral data is fit with a spectrum prediction, described by an analytical model of the β-decay spectrum and the experimental response function. The predicted detection rate $R_{\text{calc}}(\langle qU \rangle)$ is given by the convolution of the differential β-decay spectrum $R_\beta(E)$ with the experimental response function $f_{\text{calc}}(E - \langle qU \rangle)$ and the background rate R_{bg}:

$$R_{\text{calc}}(\langle qU \rangle) = A_s N_T \int R_\beta(E) f_{\text{calc}}(E - \langle qU \rangle)\, dE + R_{\text{bg}} \quad , \tag{3.5}$$

where N_T is the signal normalization derived from the number of tritium atoms in the source, the maximum acceptance angle, and detection efficiency. The factor $A_s \approx 1$ is an additional normalization parameter in the fit. The differential β-decay spectrum $R_\beta(E)$, based on

Fermi's theory, includes radiative corrections and the molecular final-state distribution. Gaussian broadenings account for Doppler broadening from the finite thermal motion of tritium molecules in the source, and energy broadenings due to spatial and temporal variations in the spectrometer and source electric potential.

Analysis of the first five KATRIN measurement campaigns yields an upper limit for the neutrino mass of $m_\nu < 0.45\,\text{eV}$ at 90% CL.[A$^+$24] Improving on previous direct neutrino mass measurements by a factor of five and reaching a world leading sensitivity in the sub-eV range.

3.2. KATRIN Main Spectrometer related background processes

For low rate experiments such as the KATRIN experiment, identifying and minimizing background contributions is of utmost importance. The applied retarding potential at the spectrometers work as an effective background rejection for any low energy backgrounds produced upstream[1] of the spectrometer section. On the other hand, any low energy background produced downstream of the analysing plane will be accelerated by the applied potential and create an event on the detector in the region of interest (ROI). In order to reach the aimed sensitivity a background rate below 0.01 cps is aimed for.[A$^+$21a]

Commissioning measurements showed a highly enlarged background rate compared to the design value. This spurred many investigations to characterize the background production mechanism and find effective counter measures. The majority of background processes are related to the large main spectrometer vessel with only a small contribution of detector backgrounds. Their sources can be categorized into four distinct production mechanism that will be further explained in the following sections. In general charged particles can also be trapped by the Penning trap formed between the pre- and main spectrometer. However, for all measurement campaigns after KNM4[A$^+$24] and all measurements presented in this work the PS voltage is set so low that backgrounds caused by inter-spectrometer Penning traps do no longer play a role. Furthermore, three Penning-wipers[A$^+$20b] have been installed preventing any Penning discharges. Therefore, the production mechanism of inter-spectrometer Penning traps is not discussed in detail.

An overview of the different remaining production mechanisms for spectrometer related backgrounds is depicted in figure 3.4. Electrons can be produced at the spectrometer surface by ambient gamma radiation or cosmic muons or by radioactive radon decays in the sensitive flux tube. Charged particles can be magnetically trapped inside the main spectrometer and ionize residual gas. The major background contribution is caused by ionization of Rydberg atoms, because they can not be effectively suppressed by implemented counter measures. This leads to the background rate exceeding the design limit by almost a factor of more than 14 for the first 5 KATRIN measurement campaigns[A$^+$24].

3.2.1. Electrons from spectrometer walls

Ambient radiation and especially the high flux of cosmic muons are problematic for all low rate experiments like KATRIN. They can produce secondary electrons on the $690\,\text{m}^2$ inner surface of the main spectrometer. Accelerated by the electrostatic potential of the MAC-E filter, these secondary electrons reach the detector with energies in the region of interest. Several efforts have been made to reduce the impact of secondary electrons on the total background rate of the KATRIN experiment.

Spectrometers of the MAC-E filter type posses intrinsic shielding against secondary electrons from their inner walls. The magnetic field lines formed by the two solenoids at the ends of

[1]The streaming direction is the one of the β electrons from the source down to the detector. 'Upstream' therefore refers to everything closer to the source and 'downstream' to everything closer to the detector

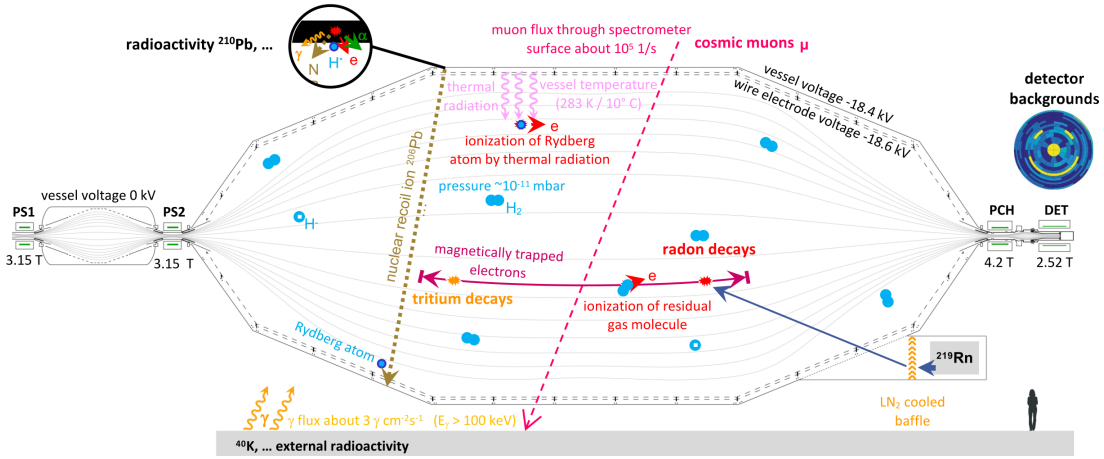

Figure 3.4.: Background production mechanisms at the KATRIN main spectrometer. Cosmic muons and ambient gamma radiation can produce secondary electrons from the inner surface of the spectrometer walls. The radioactive noble gas ^{219}Rn is emanated from the non-evaporable getter material. When it decays in the sensitive flux tube, background electrons are created that can get magnetically trapped. Implanted ^{210}Pb atoms can sputtered highly excited Rydberg atoms from the spectrometer walls that can be ionized by thermal radiation from the spectrometer vessel.

the spectrometer are almost parallel to the vessel walls. That way any charged particle from the walls is deflected by the Lorentz force providing excellent magnetic shielding. Furthermore, the KATRIN MS is equipped with an inner electrode (IE) system. Applying a negative voltage with respect to the vessel hull introduces an additional electrostatic shielding against electrons. The implementation of the wire system however further increases the surface area inside the spectrometer to a total of 1222 m^2.

To limit the impact of external radioactive sources, the floor of the main KATRIN hall was constructed using low activity concrete. Additionally, the thickness of the stainless steel spectrometer vessel was increased by 2 cm with respect to its predecessor of the Mainz experiment.[Lei14] That way, only high energetic gamma rays can penetrate deep enough into the stainless steel to produce secondary electrons on the inside of the spectrometer. Measurements performed with a ^{60}Co source directed at the outside of the MS show that ambient γ rays produce secondary electrons. They also demonstrate the effective electromagnetic shielding capabilities of the MAC-E filter in combination with an IE system.[A$^+$19b]

Cosmic muons are produced in hadronic showers and are typically shielded by placing the experimental apparatus deep underground. Due to its large size and the necessity of the tritium infrastructure this is not possible for the KATRIN experiment. Therefore, a high flux of 10^5 muons per second pass through the main spectrometer, causing ionization and excitation in the vessel. However, the aforementioned electromagnetic shielding effectively mitigates any background produced by cosmic muons.

In an effort to assess the background contribution by muon induced electrons a correlation measurement was performed. The muon flux was monitored by 9 muon detectors surrounding the main spectrometer while an asymmetric magnetic field was used to actively guide wall electrons onto the detector. These investigations[Lin15] show a clear correlation between the muon rate in the spectrometer hall and the electron rate on the FPD (see Figure 3.5).

Surprisingly, they also show that only 14.4% of the measured electrons are produced by

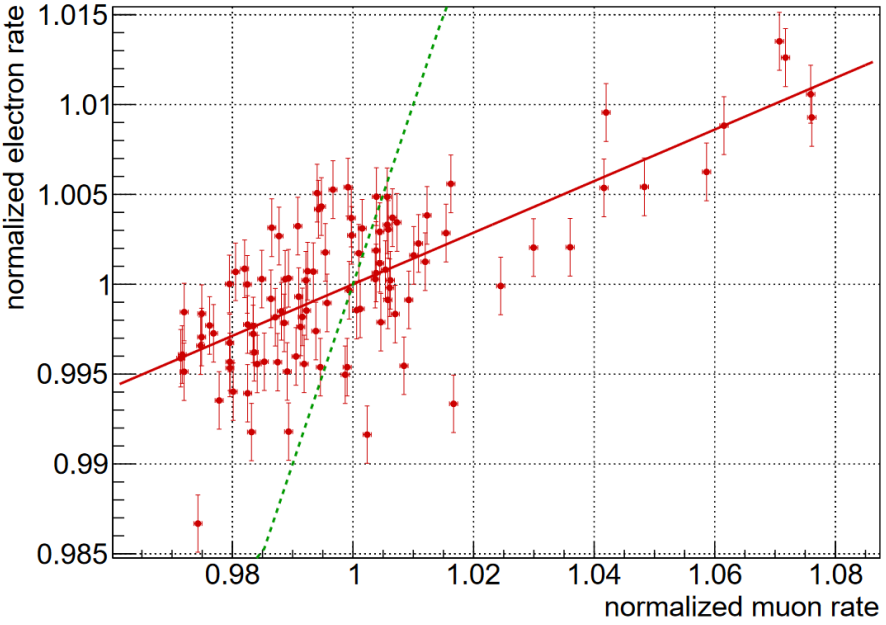

Figure 3.5.: Correlation of the muon rate in the spectrometer hall with the electron rate at the focal plane detector (solid red line). Reference for 100% muon induced events on the FPD (dashed green line)[Lin15].

muons.

Concluding, this means that secondary electrons from the main spectrometer walls are effectively mitigated by the deployed counter measures and the majority of background has to be created by a another production mechanism.

3.2.2. Radon decays

Another source of background electrons is caused by radon decays. The naturally occurring isotopes ^{219}Rn, ^{220}Rn and ^{222}Rn derived from the decay chains of uranium (^{235}U and ^{238}U) and thorium (^{232}Th), are key contributors. They are highly abundant in ambient air making up almost 50% of the worldwide mean effective dose[RS13].

In the KATRIN experiment the radon isotopes emanating from various materials within the main spectrometer, including the inner electrodes, the stainless steel vessel itself and the largest amount originates from the non-evaporable getter (NEG) strips. These NEG strips provide the major part of pumping speed to maintain the extremely high vacuum (XHV) conditions of 10^{-11} in the main spectrometer and are located in three pump ports adjacent to the main spectrometer.

To mitigate the influence of radon-induced background, liquid nitrogen-cooled baffles have been installed between the NEG pumps and the sensitive flux volume. These baffles trap radon atoms before they can enter the main spectrometer, achieving a suppression efficiency of approximately 95%.[Har15] Furthermore, the pump ports are equipped with turbomolecular pumps to effectively remove noble gas like radon isotopes. This leads to an average pump-out time of $t_{\text{pump-out}} = 360\,\text{s}$. Therefore, only the short-lived isotopes ^{219}Rn, ^{220}Rn, with half-lifes of $t_{1/2} = 3.96\,\text{s}$ and $t_{1/2} = 55.6\,\text{s}$[CER99] respectively, have a significant probability to decay within the sensitive flux tube. On the other hand, ^{222}Rn has only a relatively small probability to decay before it is pumped, due to its long half-life of $t_{1/2} = 3.82\,\text{d}$[CER99].

Once a radon α-decay happens in the sensitive flux tube, there are several ways how background electrons can be generated. Heavy α-particles or photons emitted in the

decay process are of no concern for the KATRIN background since they do not follow the magnetic field lines onto the detector. Atomic shell disturbances caused by the decay can however lead to the emission of up to 20 electrons with energies ranging between the eV (shell-reorganization electrons) and the keV (relaxation, inner-shell shake-off or conversion electrons) scale through several atomic processes (see figure 3.6). These electrons are then either guided onto the detector or they can get trapped due to the magnetic bottle effect in the main spectrometer.

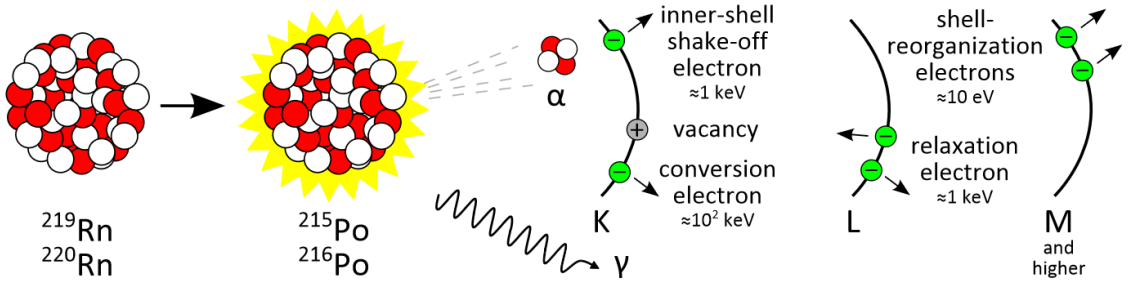

Figure 3.6.: Sketch of electron production mechanisms following radon α-decays.[Sch14]

3.2.3. Trapped electrons

Charged particles produced inside the magnetic flux tube of the main spectrometer can get magnetically trapped due to the electromagnetic-magnetic field design of MAC-E filter spectrometers. They are emitted with a polar angle θ with respect to the magnetic guide lines and are accelerated by the electrostatic potential towards either end of the spectrometer. On their way, the longitudinal component of their momentum is transformed into the transversal one and vice versa by the magnetic gradient. Since the magnetic field strength increases towards the exit of the spectrometer, charged particles moving towards the ends of the spectrometer can be reflected by the magnetic mirror effect. This effect describes the case, when a particle changes its direction, because all of its longitudinal momentum component is transformed into its transversal one. The trapping condition for particles created at position $\vec{x}$ inside the KATRIN MS is given by

$$\theta_{\max} = \sqrt{\frac{q|U(\vec{x})|}{E_{\text{kin}}(\vec{x})} \cdot \frac{B(\vec{x})}{B_{\max}}} \tag{3.6}$$

with q the electrical charge of the particle, $U(\vec{x})$ the electric potential and $B(\vec{x})$ the magnetic field at the point of creation, the kinetic energy of the particle E_{kin} and the maximal magnetic field during the particles propagation $B_{\max}$[Blo18]. These trapped particles do not only move back and forth in the axial direction, but also exhibit a slow azimuthal drift caused by radial magnetic field gradients.[Mer12][CGR06] An exemplary trajectory of a charged electron can be seen in Figure 3.7.

The trapping condition can be broken by the electrons either losing energy or changing their polar angle. Several processes can cause these changes. Electrons always lose some energy through cyclotron radiation. However, this process only plays a minor role in the KATRIN main spectrometer [M$^+$13]. The main process through which electrons are cooled down is ionization and electronic excitation via scattering on residual gas. Those collisions are so rare in the ultra high vacuum of $1 \cdot 10^{-11}$ mbar of the main spectrometer that electrons can be stored for several hours and produce hundreds of low energy secondary electrons. The number of produced secondary electrons N_S by a primary electron with energy E_{prim} is given by $N_S = \frac{E_{\text{prim}}}{\omega}$, where $\omega = 37$eV is the average energy of ion-electron pair production off H_2 for electrons[M$^+$13]. The produced low-energy secondary electrons are accelerated

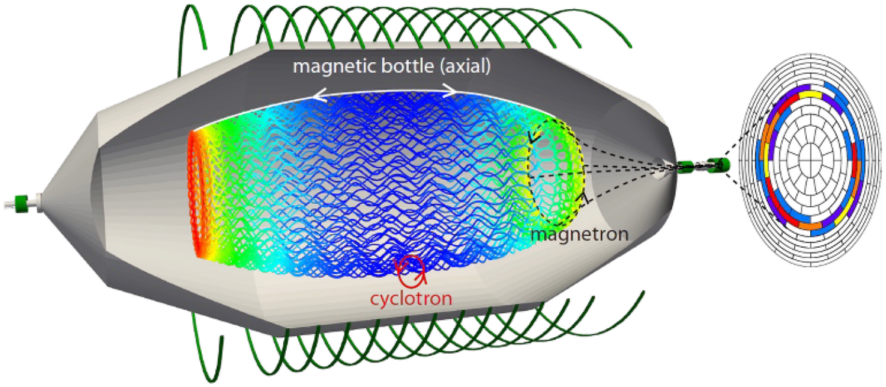

Figure 3.7.: Trajectory of a magnetically stored electron in a MAC-E filter spectrometer. The electron is reflected at both ends due to the increasing magnetic field, while also exhibiting an azimuthal drift introduced by radial magnetic field gradients.[Fra23]

towards the detector by the retarding potential and therefore create background events in the ROI on the detector. Due to the previously described magnetron drift, the signature of stored electrons can be seen by the secondary electrons producing a ring-shaped event pattern on the detector (see Figure 3.7).

For high energy electrons there are some additional breaking conditions. For example, if their transversal energy $E_\perp$ exceeds a certain threshold $E_\perp^{\max} \approx 180\,\mathrm{keV}$ the cyclotron radius is larger than the dimensions of the spectrometer. Additionally, for high kinetic energy the electrons can move non-adiabatically, which means that the change of longitudinal to transversal momentum and vice versa is no longer proportional to the change in magnetic field. Then the polar angle changes randomly and the electrons can randomly break the storage condition.

3.2.4. Rydberg background

All of the above background production mechanisms are effectively mitigated at nominal KATRIN operation. They only contribute a small amount to the overall background rate. However, the background rate still exceeds the design limit by a factor more than 14[A^+24]. This caused several investigations of the background characteristics.[Har15][Blo18] One key observation was that the KATRIN background shows a small radial dependent fraction. This can be explained by higher energetic secondary electrons produced at the spectrometer walls by muons and predominantly ^{210}Pb β decays.[Har15] These secondaries can enter the outer magnetic flux tube and cause a significant contribution to the background rate.

The majority of background events, about 75%, are however homogeneously distributed over the entire spectrometer volume. These events can not be explained by any of the previous production mechanisms. To account for the observed background dependencies the background model had to be extended. Ionization of sputtered Rydberg atoms from the spectrometer walls could explain the remaining background.[Har15, Tro19]

Rydberg atoms are atoms in exited states with at least one electron that has a high principle quantum number n. They are easily ionized which can be explained using the Bohr model[**?**]. The orbital radius r_n is given by

$$r_n = \frac{4\pi\epsilon n^2 \hbar^2}{Z m_e e^2} \tag{3.7}$$

with the vacuum permittivity ϵ, the principle quantum number n, the reduced Planck constant $\hbar$, the atomic number Z, electron mass m_e and the elementary charge e. In general

th geometric cross section scales with the orbital dimension so $\sigma \propto n^4$. Additionally, the binding energy falls off towards higher radii. For hydrogen and hydrogen-like atoms the binding energy is given by

$$E_n = -Ry\frac{Z^2}{n^2} \tag{3.8}$$

with the Rydberg energy $Ry = 13.6\,\text{eV}$. So for a hydrogen (Z=1) electron with principal number $n = 10$ for example, the geometric cross-section is enlarged by a factor of 100, while the binding energy is in the order of 0.1 eV. This means the Rydberg atoms can be ionized by the black body radiation (BBR) of the spectrometer or by the process of autoionization.[Hin22]

In the KATRIN experiment Rydberg atoms are assumed to be sputtered from the spectrometer walls. In figure 3.8 the sputtering process is shown. During the installation of the inner electrode system, the spectrometer was exposed to ambient air. This caused a contamination of the spectrometer walls with ^{210}Pb from the uranium-238 decay chain. An activity of approximately 1 kBq has accumulated.[Har15] ^{210}Pb decays into ^{210}Po via two β decays. The high energetic recoil nucleus of ^{206}Pb following the α decay of ^{210}Po scatters on the atoms in the stainless steel. Thereby atoms can be knocked out of the lattice structure and enter the spectrometer volume. When the lead nucleus is able to leave the vessel and propagate through the spectrometer volume, it can also sputter electrons from the opposite side of the spectrometer upon hitting the wall. Some of these sputtered atoms can be in highly excited states. Also atoms from gases condensed on the wall can be released via scattering and enter the volume in excited states. Since these atoms are neutral they are not effected by the electromagnetic shielding and can freely diffuse into the sensitive flux tube. If they are ionized inside the flux tube by BBR or other processes, low energy background electrons are emitted.[Har15, Tro19, Hin22]

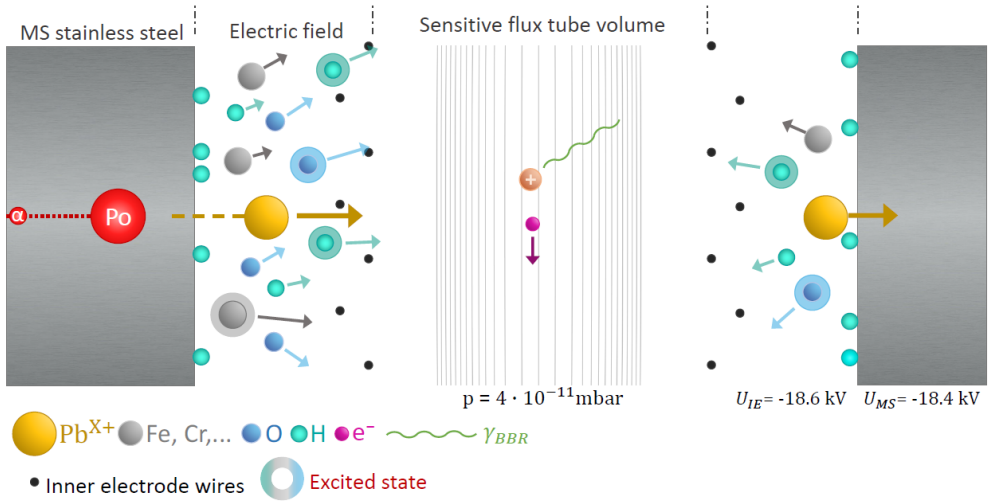

Figure 3.8.: Sputtering of Rydberg atoms from the spectrometer walls. The high energetic recoil nucleus of ^{206}Pb following the α decay of ^{210}Po scatters with the atoms inside the stainless steel spectrometer vessel and gas adsorbed to its surface. Thereby atoms are released into the spectrometer volume. Some of these atoms are in highly excited states, indicated by the shaded area surrounding the atom. The black dots depict the inner electrode wire system and the magnetic flux tube is shown as magnetic field lines. If Rydberg atoms are ionized inside this flux tube the generated electron is guided towards the detector. [Hin22]

3.3. keV-scale sterile neutrino search with the TRISTAN SDD

After completing its primary mission of determining the electron neutrino mass, the KATRIN experiment will be repurposed to search for sterile neutrinos in the keV mass range. Sterile neutrinos, which are right-handed and do not interact via the Standard Model forces, are a natural extension to the Standard Model. The existence of heavy sterile neutrinos would lead to a distinct contribution in the electron energy spectrum. This contribution is characterized by the mass of the sterile neutrino and the neutrino mixing amplitude, with the endpoint energy of this new branch given as the difference between the spectrum endpoint energy and the neutrino mass ($E_{max} = E_0 - m_s$). The superposition of this new branch with the well-known beta decay spectrum results in a kink-like feature. This feature is characterized by the mass of the sterile neutrino m_s and the mixing amplitude $\sin^2\theta$. This measurement is therefore sensitive to sterile neutrino masses up to the tritium endpoint energy $E_0 \approx 18.6\,\text{keV}$.

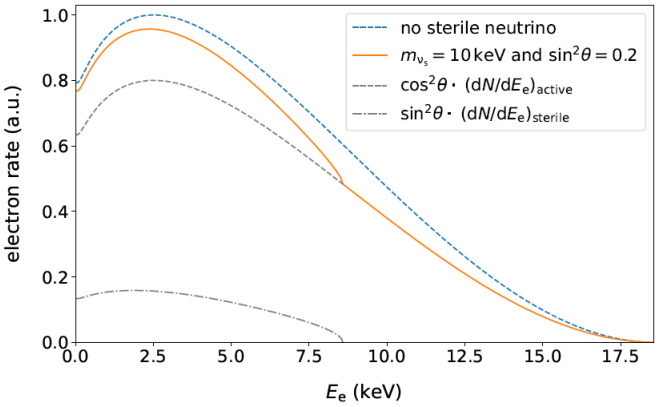

Figure 3.9.: Imprint of a sterile neutrino in the tritium β decay spectrum. The additional decay branch of a sterile neutrino leads to a characteristic kink in the decay spectrum. From the position and the magnitude of the kink, the sterile mass and its mixing angle can be inferred.[TRI21]

To detect these subtle changes, the aimed sensitivity level for the mixing amplitude is $\sin^2\theta = 10^{-6}$. This level of sensitivity surpasses previous laboratory measurements and reaches mixing amplitudes of cosmological interest. Achieving such high precision requires controlling systematic uncertainties to a very high level. The accuracy of the experiment is mainly limited by the reduction of these systematic errors.

To reach the desired sensitivity for the keV-scale sterile neutrino search, several parameters of the KATRIN experiment need to be adapted. One significant adaptation is the detector system. The retarding potential of the spectrometer will be set much lower, because the whole energy spectrum, not just the endpoint region, is of interest. Observing the whole spectrum increases the count rates of electrons passing through the spectrometer by several orders of magnitude. Additionally, the differential measurement mode is used to investigate active-to-sterile mixing, necessitating the design of a novel detector system.

The new detector must handle increased count rates of up to 1×10^8 counts per second (cps) while maintaining a high energy resolution of 300 eV at 20 keV for electrons. To meet the necessity of high count rates while keeping the pile-up probability low, a maximum of 1×10^5 cps per pixel is planned, requiring a minimum of 1000 pixels on the new detector. [TRI21]

The existing detector in the KATRIN experiment is not built to handle such high count rates or achieve such high energy resolution. Therefore, a new multi-channel silicon drift

detector (SDD) array was designed. This array will be integrated into the existing system, with considerations to minimize gas flow from the electronics side to the spectrometer side to maintain vacuum conditions and prevent surface depositions that could decrease detector sensitivity over time.

By leveraging the KATRIN infrastructure and incorporating novel detector technology, the project aims to probe sterile neutrino properties with unprecedented sensitivity, potentially uncovering new physics beyond the Standard Model.

4. Final pressure in the Main Spectrometer with TRISTAN

KATRIN neutrino mass measurements are scheduled to finish by the end of 2025. Until then KATRIN aims to reach 1000 days of data taking. After the very successful runtime of KATRIN, its well understood apparatus will be used to take a deeper look into the tritium spectrum. Therefore, the new multi-pixel high resolution TRISTAN SDD was developed [M$^+$19][TRI21]. It has an excellent energy resolution of 300 eV at 20 keV and can handle signal rates of 10^8 cps. The entire TRISTAN detector will consist of a tower of 9 TRISTAN modules (see Figure 4.1a) and is planned to replace the current KATRIN focal plane detector wafer.

The modular design of the TRISTAN detector allows for a phase-wise integration into the KATRIN beamline. This way the detector modules can be intensively studied during development, while allowing the detector to be upscaled to the desired size. However, this modular design raises issues for the vacuum compatibility of the detector. The outgassing of electronic components can significantly increase the final pressure of the main spectrometer To ensure the UHV conditions of up to 10^{-11} mbar in the MS, the gas flow from the detector section has to be below $5 \cdot 10^{-8} \frac{\text{mbar L}}{\text{s}}$[TRI21].

The scope of this work is to determine the final pressure of the main spectrometer with an integrated TRISTAN SDD in the KATRIN beamline (Figure 4.1b) using the MolFlow+[Ady] vacuum simulation software.
First, an introduction into the simulation software MolFlow+ and its key components is given in section 4.1. The vacuum system of the KATRIN spectrometer as well as the planned modifications to the vacuum system of the detector section are described in section 4.2. In section 4.3 the settings for the simulation are described. This section also explains the gas dependence of key simulation parameters and how the pressure can be determined from a TPMC (Test-Particle Monte Carlo) simulation. Section 4.4 discusses the simulation results for different simulation settings.

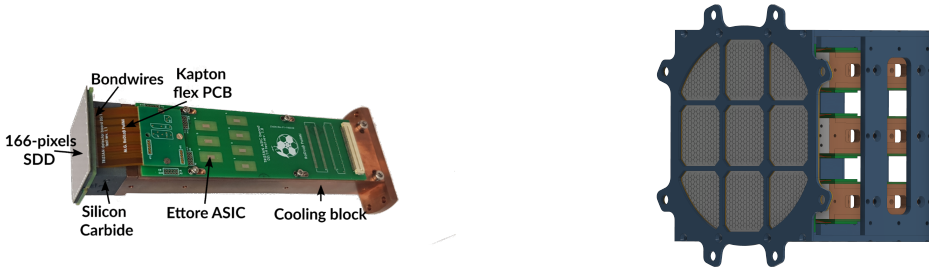

(a) Photograph of a TRISTAN detector module.[TRI21]

(b) CAD drawing of the 3x3 TRISTAN detector tower with the detector shield.

Figure 4.1.: Depiction of a single TRISTAN detector module and the complete 3x3 detector tower.

4.1. Vacuum Simulation Software MolFlow+

MolFlow+ is an advanced vacuum simulation software developed by CERN for the purpose of analyzing and optimizing vacuum systems. This software was especially developed for extremely low pressure vacuum systems, where molecular flow can be guaranteed. This section will provide a short introduction into the MolFlow+ software algorithm and is mainly based on its documentation [AKL16] and an update report presented at the 10th international particle accelerator conference [AK19].

Molecular flow assumes there are no particle interaction with residual gas molecules. This means gas molecules only interact with the surrounding walls of the gas recipient. The average distance a gas molecule travels in between collisions, the mean free path is given by

$$\lambda = \frac{k_B \cdot T}{\sqrt{2}\pi \cdot p \cdot d_m^2} \tag{4.1}$$

where k_B is the Boltzmann constant, T the gas temperature, p the pressure and d_m is the molecules diameter. So for the assumption of molecular flow, the mean free path has to be large compared to the geometrical dimensions d of the gas recipient. This condition is characterized by the Knudsen number[Pfe13]

$$Kn = \frac{\lambda}{d} \quad \text{, with} \begin{cases} Kn > 0.5 & \hat{=} \text{ molecular flow} \\ 0.01 < Kn < 0.5 & \hat{=} \text{ transitional flow} \\ Kn < 0.01 & \hat{=} \text{ viscous flow} \end{cases} \tag{4.2}$$

Under the assumption of molecular flow it is not necessary to analytically solve the gas behavior in large systems in one step. It is then possible to employ the test-particle Monte Carlo (TPMC) method to study the behavior of single gas molecules in a vacuum environment. In short, this means in a known geometry a single test-particle is created at a gas source and is tracked until it is removed by a pump. Repeating this process millions of times yields accurate predictions of pressure distributions and the effectiveness of vacuum pumps can be made.

In order to simulate the vacuum behavior a model of the geometry has to be created. Geometries in MolFlow+ are represented by polygon facets working as boundaries for particle propagation. For each individual facet a set of physical parameters can be set and the properties of the simulated particles are defined by their molecular mass. The tracking of test particles can then be split into three distinct interactions

Particle generation:
For each facet i an outgassing rate Q_i can be set. The probability $P_{\text{outgassing}}$ with which a facet is chosen as starting point of the particle is then determined by the fraction of the facets outgassing to the overall outgassing rate $P_{\text{outgassing}} = \frac{Q_i}{\sum Q_i}$. Once a facet is chosen the exact starting point is drawn from a uniform distribution over the facets area. From this point, the particles are then started with an angle θ_i with respect to the facets normal, that is distributed according to Knudsen's Cosine law[Knu09] and the particle speed v is drawn from the Maxwell-Boltzmann distribution with the temperature T_i of the facet. The trajectory of the particle is then extended until it crosses another facet and a **Facet hit** occurs.

Facet hit:
Once a particle hits a facet it can either be removed by a pump or be reflected at this facet and there are three facet counters, that are updated to later extract physical quantities of the system.

- The **Monte Carlo hit counter** $N_{\text{hit}}^{(i)}$ is incremented by one upon each facet hit. This quantity can then be used to calculate the impingement rate on this facet.
- The **total orthogonal momentum change** $\sum p_{\perp}^{(i)}$ is increased by each particles orthagonal momentum change $p_{\perp}^{(i)} = mv\cos\theta_i$ on the facet. For particle desorptions (adsorption) the momentum change is given by the orthogonal momentum of the outgoing (incoming) particle. If a particle is reflected the momenta of the incoming and outgoing particle are added. With this counter the pressure on a facet can be calculated.
- As a third counter also the sum of the **reciprocal orthogonal particle speeds** $\sum \frac{1}{v_{\perp}}$ is registered to calculate the particle density near a facet.

For diffusely reflected particles a new particle speed is drawn from the Maxwell-Boltzmann distribution and the outgoing angle θ_r is again calculated according to Knudsen's cosine law[Knu09].

Particle adsorption The probability of the particle being pumped is given by the sticking coefficient s assigned to the facet. For vacuum systems in equilibrium, the sticking coefficient s is related to the pumping speed S by

$$S\left(\frac{\mathrm{m}^3}{\mathrm{s}}\right) = s \cdot \frac{1}{4} \cdot \bar{v}\left(\frac{\mathrm{m}}{\mathrm{s}}\right) \cdot A(\mathrm{m}^2) \tag{4.3}$$

with the area A of the facet and the mean particle speed $\bar{v} = \sqrt{\frac{8k_BT}{\pi m}}$ with k_B - Boltzmann constant, T - temperature and m - molecular mass. If a particle is pumped, a new test-particle will be generated according to the procedure described under **Particle generation**.

4.2. Setup for the integrated TRISTAN detector

The scope of this work is to determine the final pressure in the MS for the integrated TRISTAN detector into the KATRIN beamline. Therefore, the geometry of the KATRIN MS up to the detector section is setup in MolFlow+. Real 3D geometries from CAD programs can be imported to MolFlow, but these geometries are often very complex and contain many non-relevant parts like screws and screw holes. Additionally, there is no CAD file of the full SDS section and it was therefore decided to set up the geometry with MolFlows' geometry editor. The MolFlow setup and its corresponding pumping layout can be seen in figure 4.2. To reduce the complexity of the system, the PS geometry is not designed, but rather an effective pumping speed towards the MS is applied.

With the geometry set, only the start and end conditions for the particles have to be set. Start conditions are given by an outgassing rate on the facets and end conditions are set by a sticking factor on the facets. This sticking factor can then be converted into a pumping speed according to equation 4.3.

4.2.1. Vacuum setup for KATRIN and simulation cross-check

In order to check the validity of the applied simplifications in the geometry and the assumed pumping speeds a comparison with the prevailing KATRIN conditions is made. For the simulation pumping facets are distributed according to the positions shown in figure 4.2b. For comparison to KATRIN-like conditions a fully reflective facet is inserted at the position of the detector shield, representing the KATRIN FPD. This facet fully separates the MS from the detector section. The final pressure of the MS is then only limited by the hydrogen outgassing of the spectrometer walls and the applied pumping speed.

For the spectrometer walls a specific outgassing rate of 1.77 $\frac{\text{mbar L}}{\text{s cm}^2}$ is assumed. The stainless steel alloy 316LN used for the construction of the spectrometer vessel as well as the inner electrode system has a specific outgassing of about $1.0 \cdot 10^{-12} \frac{\text{mbar L}}{\text{s cm}^2}$[A$^+$16]. For the simulation geometry only the inner surface area of 690 m^2 is taken into account. To include the additional area of the IE system of 532 m^2 the outgassing rate is scaled by a factor $\frac{1222}{690} \approx 1.77$.

For the pumping the following considerations are made. As mentioned before, the Pre-Spectrometer geometry is not modeled, only and effective PS pumping speed of 600 $\frac{\text{L}}{\text{s}}$[Wol] is set. Adjacent to the MS there are three pump ports (PP) each equipped with a LN_2 cooled baffle system. These baffles were installed to prevent a direct line of sight for radon emitted by the getter pumps in the PP. In order to minimize radon background (see section 3.4), while maintaining UHV conditions in the MS, the getter strips in the center PP P1 have not been installed. Therefore, the central pump port is not shown in figure 4.2b, but its geometry and the baffle are included in the simulation. The two outer pump ports P2 and P3 are each equipped with 1000 m of St707 getter strips. Each getter strip is 3 cm wide, but only coated with NEG material to a width of 2.7 cm.[A$^+$16] Accordingly all applied sticking coefficients on the getter material in the pump ports have to be reduced by 10%. For hydrogen the sticking coefficient of the St707 getter strips was determined by a separate simulation to be 2.9%[DLBM07], so a sticking of 2.61% is applied in the simulation. Each pump port is also equipped with 3 Turbovac MAG W 2200iP [TMP] with a pumping speed for hydrogen of 2100 $\frac{\text{L}}{\text{s}}$ each. Since at nominal KATRIN operation only one of those TMPs is operated, the simulation also only includes one pumping facet at each outer PP. This is already sufficient to reach the excellent vacuum conditions in the lower 10^{-11}mbar regime inside the main spectrometer.

To also reach UHV conditions in the detector section 2 Marathon CP-8 cryo pumps[cry] with pumping speeds of 2300 $\frac{\text{L}}{\text{s}}$ for hydrogen are deployed close to the FPD. The simulation only includes one of these pumps which is connected to the inner vacuum of the post acceleration electrode (PAE). Around the inner PAE tube an isolation vacuum is created by the second cryo pump. Since the surrounding tube around the PAE electrode is not included in the geometry model, the second cryo pump is also excluded from the simulation.

For a simulation of $5 \cdot 10^7$ particles with the above described settings a final pressure in the MS of $4.6 \cdot 10^{-11}$mbar is obtained. This is in very well agreement with the prevailing vacuum conditions of the MS in the lower 10^{-11}mbar regime.

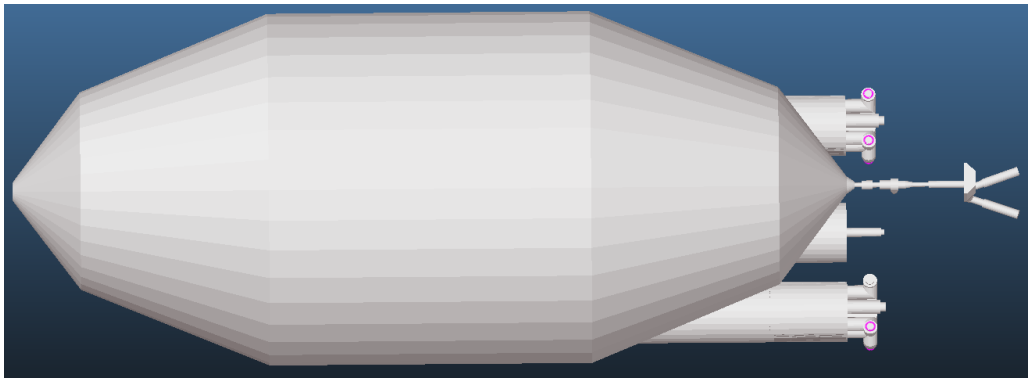

(a) SDS section geometry setup in MolFlow+.

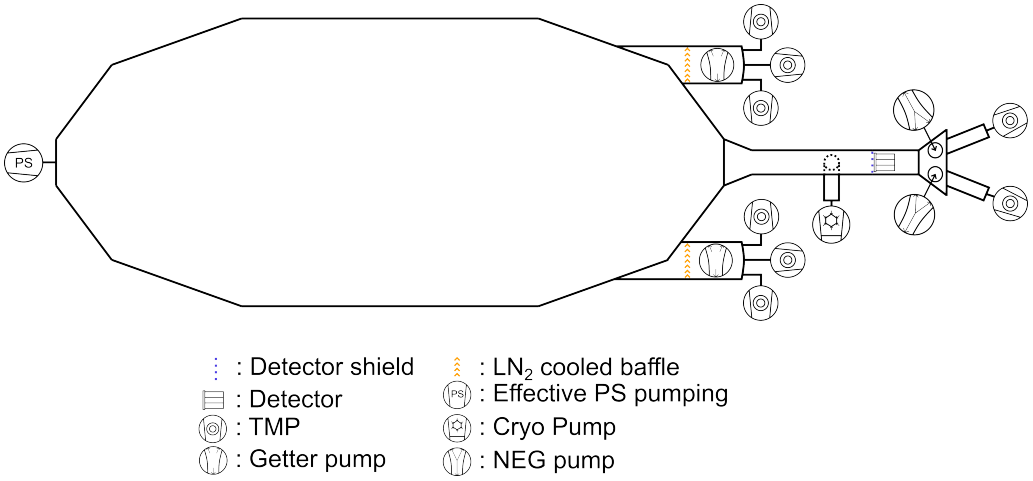

(b) Pumping layout for the MolFlow+ simulation. The center pump port is not included in the pumping layout, because there are no active pumps at this pump port. For the outer PP only one of the TMPs is actively pumping.

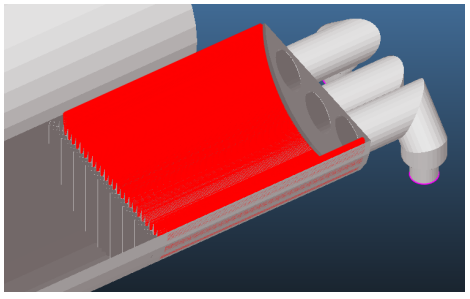

(c) Pump port geometry implemented in MolFlow+. Shown in red are the getter strips

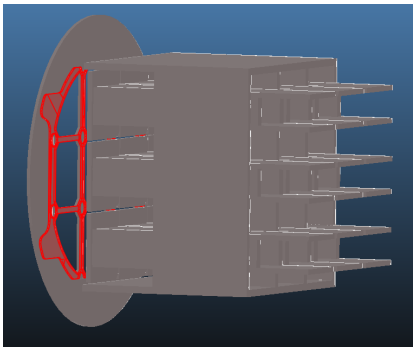

(d) Detector and shield design in MolFlow+. Highlighted in red is the aperture shown in figure 4.3a.

Figure 4.2.: Overview of the geometry and pumping for the MolFlow Simulation.

4.2.2. Vacuum changes for the integrated TRISTAN modules

With the integration of the TRISTAN modules the detector section and the main spectrometer can no longer be assumed to be fully separated. Due to the modular design, particles can pass from the electronics side through the detector towards the MS. The main limitation for the final pressure in the MS is then given by the gas flow from the detector electronics into the MS. Deteriorated vacuum conditions in the MS can lead to an influence on the quality of the measurement. Higher pressure in the MS can cause an increased background rate during the operation with the TRISTAN modules. Additionally, particles with low vapor pressures can adsorb onto the front face of the SDD wafer. This would increase the detector dead-layer over time and thereby affect the energy resolution.

In order to uphold UHV conditions in the main spectrometer the gas flow through the detector has to be below $5 \cdot 10^{-8} \frac{\text{mbar L}}{\text{s}}$[TRI21]. The gas flow through the detector is influenced by three different parameters, the gas dynamic conductance of the detector, the applied pumping speed on the electronics side and the electronics outgassing. Previous works already investigated the outgassing of the individual detector parts[Ull20] and the gasdynamic conductance of the detector[Pur22]. In the following these results are shortly summarized, but more detailed information can be found in the provided references. Also the planned changes on the vacuum system of the detector chamber are described.

Gasdynamic conductance
To prevent a direct line of sight for molecules through the detector tower a tight-fitted mechanical shield is designed. The conductance measurements showed the effectiveness of using such a detector shield that covers the gaps between individual detector modules. However, they also revealed a high dependence of the conductance on the distance between the shield and the detector front face. Figure 4.3b shows a cross-section through the detector that illustrates the distance between detector and shield. For the investigated shield design there had to be a minimal distance of 0.3 mm. This is due to bondwires connecting the SDD front face with the on-module electronics. At the closest possible distance of 0.3 mm a conductance of $C = 13.9 \frac{\text{L}}{\text{s}}$ was measured. By redesigning the detector shield this limitation is eliminated. Additional to the investigated shield that can be seen in blue in figure 4.3a, a second aperture, depicted in yellow, is made. Through this additional aperture holes are drilled to accommodate for the bondwires. The aperture is then screwed to the detector shield. Thereby, it is possible to reduce the distance between detector and shield up to zero. It also offers flexible choices for the material of the aperture. While closer distances are beneficial for the detector conductance they also introduce the risk of breaking the fragile SDD wafers during the detector tower assembly. Additionally, the distance between the shield and the detector may change when cooling down the detector. This means even with the improved shield design a minimal distance of 0.2 mm should be kept to prevent damages to the TRISTAN SDD. In the MolFlow simulation several distance settings are tested for their vacuum compatibility.

For the implementation in the simulation a simplified model of the TRISTAN modules is created with the implemented geometry editor of MolFlow+. Only the more complex shield design was imported from a STL (Standard Triangulation Language) file created with a CAD (Computer-Aided Design) software provided by Steffen Lichter. In order to reduce the computational cost of the simulation some modifications to the original shield design shown in figure 4.3a were made. First, all screw holes in the shield are removed. This reduces the amount of facets in the system that have to be tracked and drastically reduces the risk of trapping particles in the geometry. Trapping particles is a problem inherent to TPMC simulations. It means that in highly confined spaces like drill holes the test-particles can reflect between the confining walls for an indefinite amount of time without being able to reach a pumping facet and being terminated. The simulation is

stuck tracking this particle and does no longer provide any valuable information about the systems behavior. Therefore it is crucial to prevent highly confined spaces in the simulation. Furthermore, the amount of facets is reduced by omitting the exact shape of the shield and approximating its outer shape as a round disk. The exact geometry of the detector model together with the shield design optimized for the simulation in MolFlow can be seen in figure 4.2d.

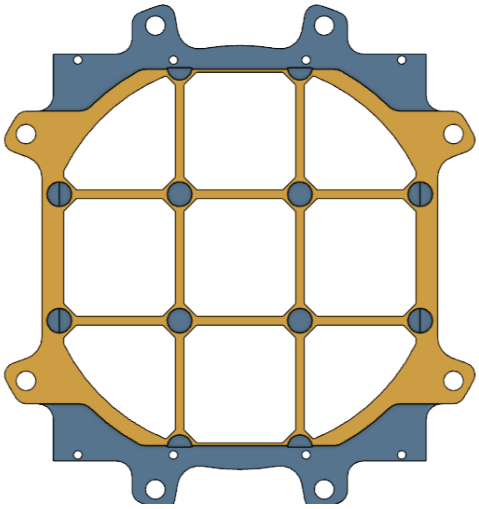

(a) Improved detector shield design. The stainless steel mechanical shield (blue) covers the gap between the detector modules and is used to mount the detector on the detector flange. A second aperture (yellow) is made to accommodate for the SDD bondwires allowing a tighter fit between the shield and the detector front face.

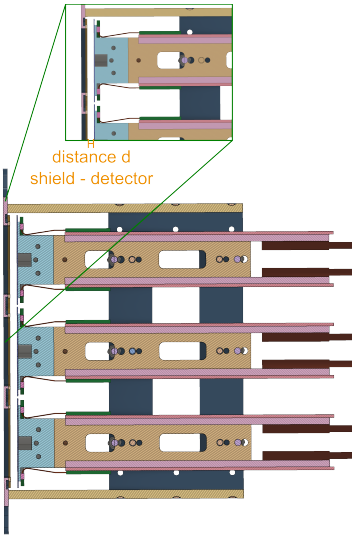

(b) Detector to shield distance. The distance is enlarged for illustrating purposes. For the integration a distance of less than 0.3mm is planned for.

Figure 4.3.: CAD drawings showing the detector shield and depicting the distance between the shield and the detector front face.

Detector side vacuum system

Another way to reduce the gas flow through the detector is to increase the pumping speed at the rear section of the detector chamber (to the right of the detector in figure 4.2b). The installed pumps have to provide at least two orders of magnitude higher effective pumping speed than the conductance toward the main spectrometer.[TRI21] For the TRISTAN detector integration an improved vacuum system is designed comprising of two CapaciTORR Z 3500 NEG pumps[NEG] and two Turbovac MAG W 2200 iP TMP's[TMP]. In the simulation the improved vacuum design is implemented to study its effect on the final pressure of the main spectrometer.

Detector outgassing

Finally, the investigated outgassing rates of the detector parts provide valuable input for the MolFlow+ simulation. In 2020 the total outgassing rate of individual detector parts have been investigated in a dedicated setup. Two independent measurement methods, the pressure increase method and the throughput method, have been used, but the pressure increase method was deemed to provide more accurate results. For the TRISTAN 100-pin flex cables only an upper limit on the outgassing could be derived, because the sample outgassing was below the outgassing rate of the measurement chamber $q_{\text{chamber}} = (1.8 \pm 0.1) \cdot 10^{-8} \frac{\text{mbar L}}{\text{s}}$. The copper block outgassing was found to be even lower with $q_{\text{copper}} = (2.0 \pm 0.9) \cdot 10^{-9} \frac{\text{mbar L}}{\text{s}}$. Due to a RGA (residual gas analyzer) malfunction the chamber outgassing decreased, allowing for the more precise measurement of copper outgassing. However, due to the lack of RGA data this measurement does not provide

any information on the gas composition of the outgassed molecules. The dominant source of outgassing is caused by the detector electronics. This comprises of a detector SDD glued to the CeSiC block and two C-shape flex PCBs together with two ASIC boards and two AirBorn 100-pin micro-D PCB connectors. Their outgassing amounts to a total of $q_{\text{electronics}} = (5.1 \pm 0.3) \cdot 10^{-7} \frac{\text{mbar L}}{\text{s}}$ and $((1.6 \pm 0.6) \cdot 10^{-6} \frac{\text{mbar L}}{\text{s}})$ for the pressure increase and throughput method respectively. This is at least 2 orders of magnitude higher than the copper block and since the chamber limits the sensitivity for the flex cables there is no reliable result on their total outgassing. Therefore, in the simulation only the electronic parts mentioned above are considered to contribute to detector outgassing. Fortunately, a representative RGA spectrum that is shown in figure 4.4 was recorded for the electronics measurement. It clearly shows the contribution of hydrogen (mass 2), methane (mass 14, 15, 16), water (mass 17, 18), nitrogen (mass 28) and carbondioxide (mass 44). The RGA was not calibrated on the overall pressure, since the main goal was only to determine the overall outgassing rate. Its spectrum can still be used to determine the fraction of each gas type on the total pressure.

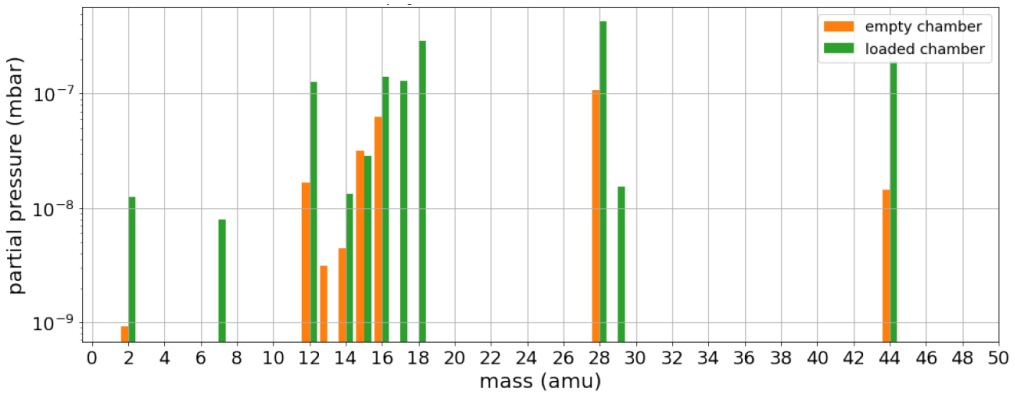

Figure 4.4.: Residual gas spectrum for the outgassing of the detector electronics. The spectrum shows contributions of hydrogen, methane, water, nitrogen and carbondioxide.

4.3. Simulation of the vacuum conditions with an integrated TRISTAN detector

MolFlow+ as a TPMC simulation can only simulate a single gas type at a time. For each detector distance the geometry has to be adjusted, so for each setting a new simulation has to be started. In order to accurately predict the prevailing pressure in the MS with an integrated TRISTAN detector at different distances a total of $n_{\text{gas}} \cdot n_{\text{distances}}$ simulations have to be performed. This means for the five different gas species emitted by the detector and e.g. 5 distance settings a total of 25 simulations have to be performed. For each of these simulations gas dependent settings like the particle mass, the outgassing value and the pumping speeds need to be adjusted. If the simulations are performed within the MolFlow+ graphical user interface (GUI), each simulation has to be started manually.

To effectively simulate the overall vacuum condition in the main spectrometer the new[1] MolFlowCLI[2] (command line interface) application was used. This way gas dependent parameters can easily be adjusted and sets of simulations can be started via simple python loops. However, all post-processing in MolFlow is still only performed inside the GUI. For a multitude of different simulations in the same geometry, the usage of the GUI to extract physical information is not very effective, so the post-processing is also performed outside

[1] Implemented since version 2.9.0

[2] Documentation for the MolFlowCLI application can be found at `https://molflow.docs.cern.ch/guide/molflow/features/molflow_cli/`

the GUI. The following section describes how gas dependent parameters are handled and implemented in the simulation and how the pressure in the system is calculated. For all setups and simulations throughout this work MolFlow+ version 2.9.18_beta[3] up to version 2.9.24 was used and tested.

First and foremost the geometry described in the previous section and shown in figure 4.2a is setup in the MolFlow+ geometry editor. Facets in MolFlow+ only have a numerical identifier, but the software also offers the possibility to save a selection of one or multiple facets under a descriptive name for fast an easy access. Therefore, all relevant facets like pumps, the detector and its electronics are saved as facet selections. This allows to make modifications in the system more intuitively. A complete list of the facet selections and their corresponding facets can be found in Appendix A.

As key input parameters the start and end conditions or rather the outgassing and pumping speeds have to be set. Both of these parameters are dependent on the gas or rather gas mass. In the following their dependencies are discussed and it is explained how they are handled in the simulation.

4.3.1. Dependence of key parameters on the molecular mass

Pumping speeds

Pumping speeds are provided in the respective data sheets of the individual pumps. These data sheets commonly only include pumping speeds for a small range of common gases in vacuum systems like hydrogen and nitrogen. Sometimes they also include water, but for other gases like methane and carbondioxide there is no information given by the manufacturers. Pumping values of turbo-molecular pumps (TMP) for any molecular mass can be extrapolated from the nitrogen (M=28) value according to an empirical formula

$$S(M) = S(M = 28) \cdot \sqrt{\frac{28}{M}} \frac{\log M}{\log 28} \tag{4.4}$$

This formula is derived from equation 4.3 for smooth sticking probabilities in a log-linear representation over the molecular mass.[Mal07] For all simulations presented here this formula was also used to extrapolate unknown pumping properties of the cryo pump and the NEG pumps. With the exception of water that can easily condensate on the cold surface of the cryo pump, the sticking probabilities show a smooth line in the log-linear representation. The NEG pumps that are pumping through chemisorption do not show the same smooth behavior of sticking probabilities. Their pumping speeds are still extrapolated with the same formula and the effect of any mismodelling is checked by varying the extrapolated pumping values. For the assumed pumping of the pre-spectrometer and the getter strips there is no information on pumping speeds by the manufacturer. In the case of the pre-spectrometer there is an estimated pumping speed for hydrogen. This value is transferred to a sticking probability using equation 4.3. By keeping a fixed sticking value, while changing the molecular mass in the simulation the pumping speed behaves like

$$S(M) = S(M = 28) \cdot \sqrt{\frac{28}{M}} \tag{4.5}$$

due to the changed molecular speed in equation 4.3. The sticking probability that is derived for hydrogen on the getter in the PP is also fixed in the simulation and the pumping speed will decrease accordingly. Table 4.1 summarizes how the individual pumping speeds for the simulation are determined for each gas type.

[3] Actually a modified version of v2.9.18_beta was used. It can be found and downloaded from the 'build-artifact' column for different operating systems at `https://gitlab.cern.ch/molflow_synrad/molflow/-/pipelines/6709011`

Outgassing parameters
For the simulated system there are two main contributors to the overall outgassing. First, hydrogen desorption from the stainless steel spectrometer vessel provides the main pressure limitation for KATRIN, as already demonstrated in section 4.2.1. Once the TRISTAN detector is integrated into the KATRIN beamline, the detector electronics will add to the overall outgassing rate. The outgassing rate at the detector will however differ depending on the gas type. The gas dependent outgassing rate of the TRISTAN modules is determined based on the residual gas spectrum shown in figure 4.4. Since the RGA was not calibrated for different gases before the measurement, this spectrum is only used to extract some estimate for the fraction of each gas in the residual gas. This fraction is then scaled by the total outgassing. For the total outgassing the results from the throughput method with $q_{\text{electronics}} = (1.6 \pm 0.6) \cdot 10^{-6} \frac{\text{mbar L}}{\text{s}}$ are used. As they yield the higher outgassing value this will display an upper limit on the obtained pressure for each scenario.

To determine the fractional gas composition the emitted gas spectrum given by the loaded chamber measurement is first corrected for the residual gas spectrum of the empty chamber. This is done by simply subtracting the two spectra from each other. For each gas type a number of mass peaks can contribute. In the RGA the gas is ionized and in that process molecules can also fraction. Methane for example with a mass of M(CH_4)=16 u does not only contribute to the peak at mass position 16, but also contributes a non-negligible amount to the peaks at mass position M(CH_3)=15 u and M(CH_2)=14 u. This fact makes the evaluation of RGA spectra a non-trivial task and for the case of the uncalibrated spectrum some simplifications are made. Each mass peak is fully assigned to the gas that poses the major contribution in its fractioning ratio. This can be justified, because the fraction ratios are in general at least one order of magnitude lower than the main peak and all errors can then be assumed to be in the order of 10% or lower. As mentioned before, the residual gas spectrum was not calibrated and the measurement was performed using detector parts from the first revision that have been changed. The error resulting from the performed simplifications are thus small against the systematic uncertainties of the underlying spectrum. The peaks are then assigned to each gas according to table 4.2. Remaining peaks that can not be properly assigned to any gas are excluded from further analysis. The fraction of a gas is determined by the fraction of the sum of all partial pressures assigned to a gas and the sum of all partial pressures in the spectrum.

In order to have more reliable information on the detector outgassing new measurements at an improved test stand with the newest revision of detector parts are planned. For the input of future simulations it would be beneficial to perform dedicated measurements of the gas composition emitted by the detector parts.

With all relevant input parameters of the vacuum system determined the simulations can be performed for each gas type individually. Each partial pressure obtained from the

Table 4.1.: Summary of how the pumping speeds of the pumps are obtained for each gas type. Extrapolation of pumping speeds is calculated according to an empirical formula given in equation 4.4.

	Gas type				
Vacuum pump	H_2	H_2O	N_2	CO_2	CH_4
PS	fixed sticking of 0.069 corresponds to H_2 pumping speed				
PP getter	fixed sticking of 0.0261 determined for H_2				not getterable
TMP	data sh.	extrapolated	data sh.	extrapolated	extrapolated
cryo	data sh.	data sh.	data sh.	extrapolated	extrapolated
NEG pump	data sh.	data sh.	data sh.	extrapolated	not getterable

individual simulations contributes to the prevailing total pressure in the main spectrometer. How the pressure is calculated from the results of a TPMC simulation will be discussed in the following.

4.3.2. Pressure determination for MolFlow+ simulations

In MolFlow+ each facet is a planar polygon in a cartesian coordinate system. The position of each corner is defined by a vertex representing the coordinates of this point in 3 dimensional space. To determine the area of a facet with n vertices it is split into $n-2$ triangles. The area of each triangle is then simply determined as half the norm of the cross product between its spanning vectors and the total area of the facet is determined by

$$A = \frac{1}{2}\left\|\left(\sum_{k=1}^{n-1} \overrightarrow{v_1 v_k} \times \overrightarrow{v_1 v_{k+1}}\right)\right\| \tag{4.6}$$

with v_k representing the coordinates of vertex k. Every particle adsorbed, desorpt or reflected at a facet of area A exerts a force onto this facet, that is tracked via a counter of the total orthogonal momentum change $\sum p_\perp$ for each facet. The pressure P on any facet can then be calculated as

$$P = \frac{F}{A} = \frac{\sum p_\perp}{A} \cdot K_{\frac{\text{real}}{\text{virtual}}} \tag{4.7}$$

with $K_{\frac{\text{real}}{\text{virtual}}}$ as the flux of real particles that is represented by each test particle. This factor is necessary, because even low outgassing rates of $10^{-7}\,\frac{\text{mbar L}}{\text{s}}$ correspond to a particle influx in the order of 10^{12} particles per second. Due to computational limitations not all of these particles can be tracked, so each virtual particle N_{virtual} that is simulated and exerts a force represents a flux of real particles entering the system $K_{\frac{\text{real}}{\text{virtual}}} = \frac{n_{\text{real}}/dt}{N_{\text{virtual}}}$. The overall particle influx is calculated from the derivative of the ideal gas equation

$$\frac{dn_{\text{real}}}{dt} = \frac{\frac{d(PV)}{dt}}{k_B \cdot T} = \frac{\sum Q_f}{k_B \cdot T_f} \tag{4.8}$$

where P is the pressure, V the volume, k_B is the Boltzmann constant, T is the pressure and Q is the outgassing rate. The subscript f shows that this value is facet dependent in the simulation and to derive the factor $K_{\frac{\text{real}}{\text{virtual}}}$ the sum of all outgassing facets of the system have to be considered.

4.4. Simulation results

First a simulation with nitrogen was performed to find the optimal number of simulated particles. Therefore, the pressure was evaluated at 4 representative positions in the system for a varying number of simulated particles. The number of desorbed particles are chosen logarithmic from $1 \cdot 10^6 - 1 \cdot 10^8$. The evaluated facets are highlighted on the left hand side of figure 4.5 and their corresponding pressure evolution is shown on the right side.

Table 4.2.: Mass peaks assigned to individual gas types in the RGA spectrum.

Gas	H_2	CH_4	H_2O	N_2	CO
Assigned mass peak	2	14,15,16	17,18	28,29	44

It can be seen that the pressure converges quite fast for most of the facets. Even for 10^6 particles the pressure deviation is below 5% for all investigated facets. Especially, the pressure on the downstream side of the detector already obtains consistent results for one million simulated particles. This is expected considering that all particles start from detector facets and therefore almost all simulated particles hit this facet. For all other facets there is a significant chance that particles are pumped out of the system before they hit the facet. This reduces the statistics for the simulated pressure on these facets. In particular the extractor gauge that is located at the pump port behind the baffle and the getter strips is subject to this statistic reduction. To ensure that reliable pressure results can be obtained even for different pumping speeds, while keeping the computational time of each simulation in a reasonable range of several hours[4] $5 \cdot 10^7$ particles are tracked in each simulation.

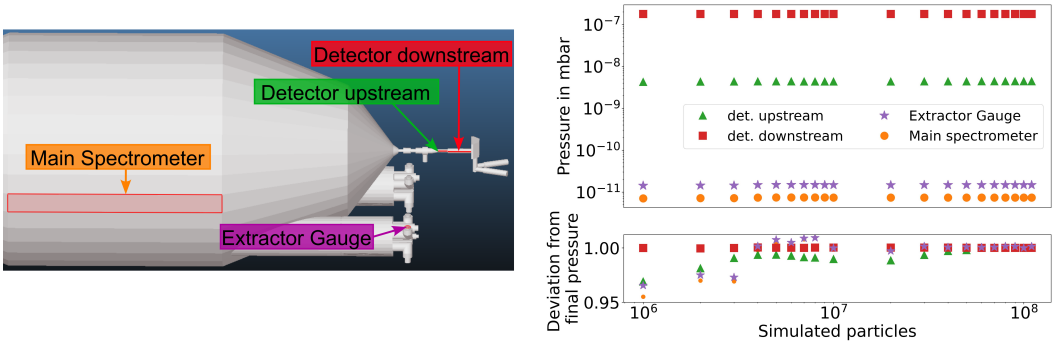

(a) **(b)**

Figure 4.5.: Pressure convergence corresponding to the amount of simulated particles.

Now to properly assess the final pressure in the main spectrometer a simulation is performed for each gas type emitted by the detector. All gas dependent parameters are adjusted as described in section 4.3.1 between the individual simulations and for hydrogen the outgassing of the stainless steel vessel is also taken into account. Additionally, the effect of the distance between the detector and the mechanical shield (figure 4.3b) is investigated by increasing the detector distance from 100 µm to 500 µm in steps of 100 µm in the simulations. The total pressure is then calculated as the sum of partial pressures exerted by every gas type.

The prevailing pressure conditions in the main spectrometer and in front of the detector for varying distances can be seen in figure 4.6. There is no significant pressure increase compared to the nominal KATRIN pressure of $1 \cdot 10^{-11}$ mbar. Furthermore, the results show a surprisingly low dependence on the detector distance. This means, the planned improvements on the vacuum system on the detector side effectively reduce the gas flow towards the main spectrometer and might allow for higher detector distances. However, the pressure in front of the detector is in the order of $1 \cdot 10^{-9}$ mbar and exhibits a higher dependence on the detector distance. With higher pressures close to the cooled detector front, particles of gases with low vapor pressure can adhere on the SDD front face and increase the dead-layer. This would lead to deteriorated detector resolution over time influencing the sensitivity of the sterile neutrino analysis. Further studies of the adsorption on the detector front face have to be performed to assess the impact of the detector distance on the dead-layer increase.

[4]The duration of a simulation not only depends on the amount of simulated particles, but also on the time each particle is tracked before it is removed. Therefore, the pumping speed also impacts the simulation time.

However, the presented results have to be treated carefully since some of the input parameters have not been determined in dedicated measurements or had to be extrapolated. To illustrate the deviations that can arise from the extrapolation of pumping speeds for unknown gases another set of simulations was performed. This time all extrapolated values (see 4.1) are reduced (increased) by 20% of the extrapolated value, which results in the deviation from the final pressure indicated as error bars. Overall the pressure changes only slightly with this modification. Since there is at the time no handle on how far the real pumping speeds deviate from the simple extrapolation performed for the inputs, the pressure situation could be much worse. For 50% reduced pumping speeds of the extrapolated values, shown as orange dashed lines in figure 4.6, the pressure still remains in the 10^{-11}mbar regime. For a more drastic situation, where the pumping speeds of the extrapolated values are reduced an order of magnitude, given by the green line, the overall pressure also increases about an order of magnitude. What can also be seen for these worse case estimations is that for lower pumping speeds the pressure becomes more and more dependent on the detector distance. This can be explained by the affected pumps. Most of those pumps that are affected by changes of the extrapolated values are located at the detector chamber. If the gases emitted by the detector are not effectively pumped they are more likely to diffuse in the spectrometer and increase the overall pressure.

Therefore, it is important to refine the input parameters for the simulation. Dedicated measurements of the gas dependent outgassing of the individual detector parts are essential to obtain reliable simulation results and accurate predictions for the main spectrometer pressure. Additionally, determining the pumping speed of the NEG pumps and TMPs that will be added to the detector side for all relevant gases further improves the reliability of the simulations.
In this work it was demonstrated, that the pressure inside the main spectrometer at nominal KATRIN operation can be accurately reproduced by vacuum simulations with MolFlow+. These simulations can also be used to predict the pressure in the MS with integrated TRISTAN modules. To obtain reliable predictions the gas dependent outgassing of the detector needs to be determined in a dedicated measurement. The accuracy of the extrapolated pumping speeds for methane and carbondioxide should also be further investigated to reduce uncertainties of the simulation results.

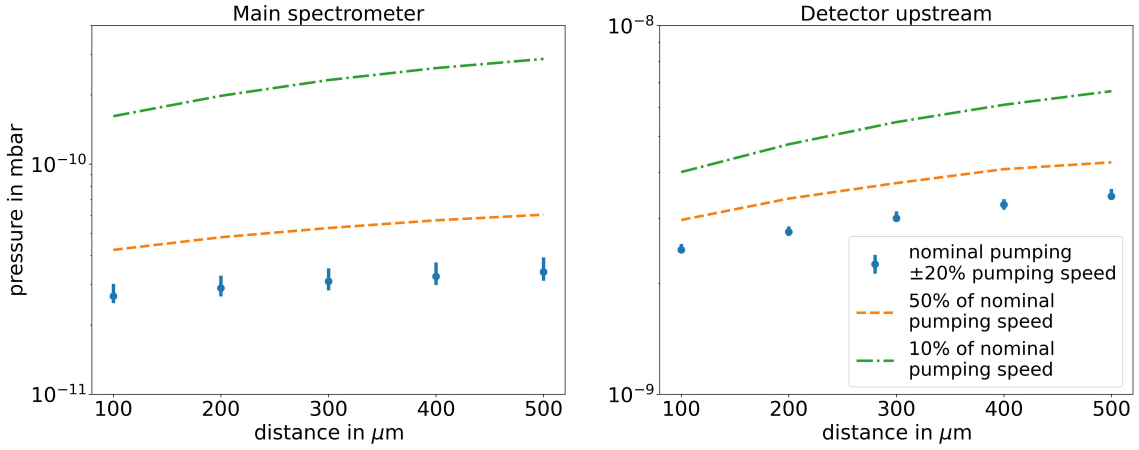

Figure 4.6.: Pressure in the main spectrometer with the TRISTAN modules.

5. Exploratory background measurements at higher pressure

Extending KATRIN with the TRISTAN detector in order to search for keV-sterile neutrinos involves several changes to the KATRIN beamline. In particular the electro-magnetic (EM) settings have to be changed. To allow a closer look into the tritium spectrum a lower retarding potential has to be applied at the high-pass filter of the main spectrometer. This allows electrons with lower kinetic energies to reach the detector. However, this will also cause electrons to enter the main spectrometer with high excess energies. For these electrons adiabatic transport can no longer be guaranteed. Non-adiabatic transport effects can in turn be minimized by increasing the magnetic field strength in the analyzing plane of the main spectrometer. The thereby caused reduction of the MS energy resolution does not pose an issue, because a newly designed high resolution SDD will replace the current KATRIN focal plane detector (FPD). However, with the modular design of this new detector the vacuum conditions in the main spectrometer might be deteriorated as demonstrated in the previous section. This deterioration of the vacuum conditions together with the changes in the EM design pose highly different conditions for backgrounds related to the main spectrometer.

To estimate the impact of those changes with respect to the overall background level exploratory background measurements are performed at TRISTAN-like conditions. These investigations are deemed exploratory, because the exact EM settings for the operation with TRISTAN modules are not yet determined. Additionally, the investigations are performed with the current KATRIN FPD and post acceleration electrode prior to any hardware changes in the detector section.

In the following the measurement settings for the background investigations are described in section 5.1. The resulting background energy distributions will then be discussed in section 5.2. These energy distributions have shown some unexpected features at low retarding energies. Therefore, another set of background measurements at lower retarding energies has been performed and their results are discussed in section 5.3. Some possible explanations for the observed deviations are outlined in section 5.4

5.1. Background measurement settings

Goal of the exploratory background measurements is to determine the overall background level that can be expected from the spectrometer for measurements with TRISTAN modules. Furthermore, the energy distribution of said background is of particular interest for the differential measurement mode that will be used for the keV-sterile neutrino search. The main changes to the SDS settings that have to be taken into account for the measurements are the

- deteriorated vacuum conditions in the main spectrometer
- lower retarding potential applied to the MS
- increased magnetic field strength in the analyzing plane

Additionally, there are changes that will affect the background which can not be reproduced at the moment. For all measurements the current KATRIN FPD as well as the current design of the post-acceleration electrode (PAE) are used. In this section the individual hardware components are briefly described and their settings for the measurement are explained.

First, only the SDS is used for the measurement by closing valve V4 between the CPS and the PS. Thereby separating all source and transport related parts of the experiment from the spectrometers. This is necessary because during nominal KATRIN operation tritium accumulates on the gold-plated rear wall. Once the tritium decays, beta electrons are emitted and guided towards the detector. Even with an empty source the rear wall activity would make a measurement of purely background events impossible. Additionally, for low retarding energies in the spectrometers the electron rates from the rear wall can cause problems at the current KATRIN FPD. High rates of several tens of thousand counts per second can cause significant distortions in the recorded rate spectra.[A$^+$15] By closing the valve all these effects can be avoided.

Retarding potential of the MS
To generate the electric potential inside the spectrometer the vessel itself is set on high voltage. Additionally, the inside of the spectrometer walls is equipped with an IE system to fine shape the electric field (see figure 5.1) and to reduce background emitted from the spectrometer walls. During the background measurements the inner electrode offset is chosen to be -200 V. This means the inner electrode wires are set to a potential 200 V more negative than the vessel itself. For example for a retarding energy of 1 keV, the vessel is only set to -800 V, while the IE is set to -1 kV. That way secondary electrons created on the spectrometer surface by ambient gamma radiation or cosmic muons are rejected, because they typically only have energies up to several eV.

Again the exact settings for the investigations with the TRISTAN SDD are no yet set, but to take a deeper look into the tritium β-spectrum and to increase the observed keV-sterile mass range a retarding energy well below the tritium endpoint of approximately 18.6 keV is anticipated. In order to test the dependence of the background rate on the retarding potential setpoints at 1.0 keV, 10.0 keV and 18.6 keV for the measurements are chosen. This covers a wide range of retarding energies, while keeping the measurement time at a reasonable level. During the measurement each setpoint is measured for two hours before changing to the next setpoint. This process is repeated in an iterative manner. By changing the retarding potential more frequently any possible long term changes of the background rate are equally distributed over all setpoints. This effectively mitigates long term effects when comparing the different setpoint data.

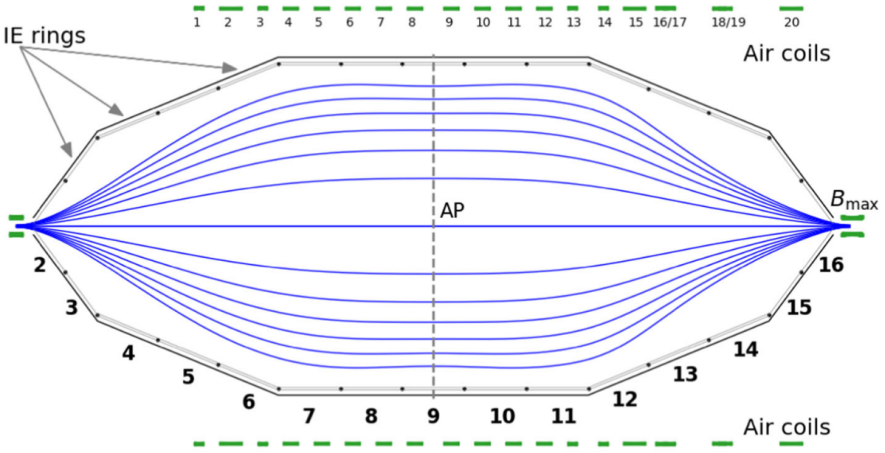

Figure 5.1.: Sketch of the main spectrometer electromagnetic layout. The air coils with their corresponding index are shown in green and the IE system is depicted as gray lines around the inside of the spectrometer.

Vacuum condition of the MS

The vacuum system of the KATRIN experiment is described in more detail in section 4.2.1. Here only the most important vacuum components will be briefly summarized. The vacuum in the main spectrometer is mainly created by a set of getter pumps and TMPs located in the pump ports of the main spectrometer. In addition there are two cryo pumps positioned close to the FPD. With this pumping system a pressure in the lower 10^{-11}mbar can be achieved inside the MS. To monitor the pressure in the main spectrometer pressure gauges are installed at each pump port. In the following all reported pressure readings are taken from the Extractor gauge (432-RPI-3-1110) at the central pump port P1.

As determined by simulations presented in the previous section vacuum conditions of the MS might deteriorate due to the integration of the TRISTAN SDD. The simulations, however also suggest, that with sufficient pumping on the detector side vacuum conditions in the spectrometer can be kept close to the nominal KATRIN pressure. Therefore background measurements at each retarding energy setpoint are performed for two different pressure settings. First, they are performed at nominal KATRIN pressure of $1.8 \cdot 10^{-11}$mbar. Then the pressure is artificially increased to $9.8 \cdot 10^{-10}$mbar by injecting helium gas into the main spectrometer. Injection of the gas is performed in static mode. This means that prior to the gas injection valves in front of all TMPs and the FPD cryo pumps are closed to decouple the pumps from the SDS beamline. The getter pumps can not be decoupled, however this is also not necessary because helium is an inert gas that is not effectively removed by getter pumps.

Magnetic field in the MS

The magnetic field is mainly shaped by the two SDS solenoids at each end of the spectrometer operated at their nominal setting. The PS2 magnet, that is located between the PS and the MS is set to $B_{\mathrm{PS2}} = 3.1\,\mathrm{T}$, while the pinch magnet is set to $B_{\mathrm{PCH}} = 4.2\,\mathrm{T}$. In order to fine tune the magnetic flux tube, the main spectrometer is equipped with an air coil system surrounding the spectrometer vessel. The air coil system comprises of the EMCS (Earth Magnetic field Compensation System) and the LFCS (Low Field Correction System). Since the EMCS is only used to compensate for the earth magnetic field its settings are not changed for the measurement. The LFCS on the other hand is used to shape the magnetic field in the main spectrometer. Therefore, 20 air coils[Hub21], each equipped with a separate power supply, are coaxially aligned with the spectrometer axis (see figure 5.1). By changing the current through each air coil it is possible to tune the magnetic field to the desired strength and shape.[GDL+13][E+18] For measurements with the TRISTAN SDD

the minimal magnetic field in the analyzing plane has to be increased to ensure adiabatic transport.[TRI21] The exact magnetic field is not yet set, but previous investigations suggest that the air coils should be operated with their maximal current or even higher.[Hub15] Consequently, the maximal symmetric field setting is used for all background measurements. Symmetric means that the analyzing plane is in the center of the spectrometer and the exact current settings for each coil can be found in table 5.1. With this setting a magnetic field of 17.4 G in the AP is achieved.

Table 5.1.: Air coil currents for the background measurements

air coil index	1	2	3	4	5	6	7	8	9	10
current I (A)	120	120	110	110	110	110	100	110	110	110
air coil index	11	12	13	14	15	16	17	18	19	20
current I (A)	110	110	110	110	80	85	85	85	-75	-120

Focal Plane Detector system

Electrons passing through the MS enter the focal plane detector system shown in figure 5.2. They are collimated and guided by the pinch and detector magnet onto the detector wafer. Before reaching the detector the guiding magnetic flux tube is fully contained within the post acceleration electrode. This electrode can be used to accelerate the electrons in order to reduce detector related systematic effects like energy loss in the dead-layer and backscattering from the detector.[Des24] The current electrode design is limited to a post-acceleration voltage of +12 kV and is commonly set to +10 kV.[A$^+$15] This means the energy of detected electrons is increased by 10 keV. Together with the integration of the TRISTAN detector the PAE design is planned to be improved allowing voltages up to +20 kV.[Hil]

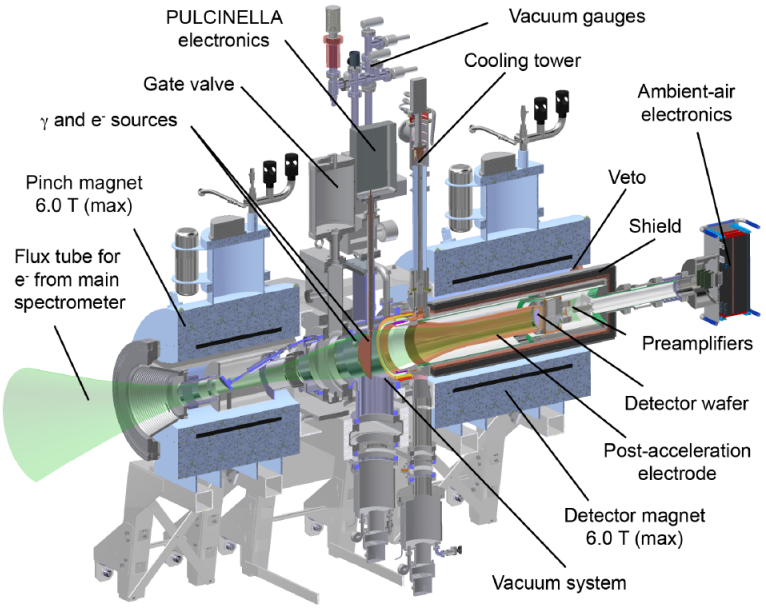

Figure 5.2.: Main components of the FPD system. Electrons enter the system from the main spectrometer on the left.[A$^+$15]

The detector itself is a monolithic 148-pixel p-i-n diode array on a single silicon wafer. It has a sensitive area of 90 mm and each pixel has a size of 44 mm^2. These pixels can be grouped into 12 concentric rings of equal size. Each ring is made out of 12 pixels and 4 pixels make up the center bull's eye of the detector. This segmentation allows corrections

of radial dependent inhomogeneities in the electric or magnetic fields. In order to reduce backgrounds produced in close proximity to the detector a passive two-layer shield is fitted within the warm-bore surrounding the detector. The outer layer is made out of a 3 cm thick lead layer to reduce γ backgrounds and an inner layer of oxygen-free high-conductivity copper to block lead X-rays. Around the passive shield a muon veto system is installed. Eight plastic scintillator panels are used to identify muon events by requiring inter-panel coincidence. Using the veto muon-induced electron events can be rejected. For the integral measurement mode with the MAC-E filter spectrometer the detector is optimized for high electron detection efficiency $> 95\%$ and not for high energy resolution. The detector still has a mean energy resolution for all pixel of 1.85 keV at the 59.54 keV line of ^{141}Am.

5.2. Investigation of background energy distribution

In total six background measurements are performed with two different settings for the pressure ($9.8 \cdot 10^{-10}$mbar and $1.8 \cdot 10^{-11}$mbar) and three different retarding energies (1.0keV, 10.0keV, 18.6keV) to study their effect on the measured background rate and energy distribution. The measurement time per setting did vary, because some measurements were performed during the week and some measurements could be performed over the weekend. The total measurement time spent at each setting is given in table 5.2. Before the anaylsis a muon veto cut is applied rejecting any events coincident within 1 µs of a muon event registered at the detector muon veto.

Table 5.2.: Measurement time in hours spent at each retarding energy

	1.0 keV	10.0 keV	18.6 keV
Nominal pressure	6 h	6 h	6 h
Elevated pressure	24 h	22 h	22 h

Goal of the measurement is to determine the energy distribution of background events. On the detector energies in the range from 6 keV to over 250 keV are measured, but for the analysis the energy range will be limited to a ROI (region of interest) from 8 keV to 32 keV. The lower limit is chosen because for energies below 8 keV a significant amount of detector noise contributes to the observed rates. The upper limit corresponds to the KATRIN ROI of KNM1 and KN2 and is chosen because it is well enough above the energy of electrons from the tritium endpoint[1]. With the high resolution TRISTAN SDD any energies above the tritium endpoint are likely to be excluded from analysis as well. For all events an energy binning of 250 eV intervals is applied to observe a significant amount of events per bin even for expected background rates of $\mathcal{O}(100)$ mcps[A$^+$24]. The background rate per energy bin is then calculated by dividing the number of entries by the total measurement time. Figure 5.3 shows the energy distribution of background rates.

All distributions show the same behavior with a gaussian peak shape around an energy of $q \cdot (U_{\text{ret}} + U_{\text{PAE}})$. This is expected since most background electrons are generated with energies in the lower eV. If they are generated upstream of the AP they get accelerated by the retarding potential U_{ret} towards the detector. Inside the PAE they are further accelerated by the potential U_{PAE}, before they reach the detector. Each distribution is fit with an empirical model

$$R = a_G \cdot \exp\left(\frac{-(E-\mu)^2}{2\sigma^2}\right) + a_E \cdot \exp\left(\frac{-(E-\mu)}{\beta_E}\right) \cdot \operatorname{erfc}\left(\frac{E-\mu}{\sqrt{2}\sigma} + \frac{\sigma}{\sqrt{2}\beta_E}\right) \tag{5.1}$$

[1]For the energy measured on the detector the shift of 10 keV caused by the PAE has to be taken into account, so the tritium endpoint on the detector corresponds to an energy of approximately 28.6 keV

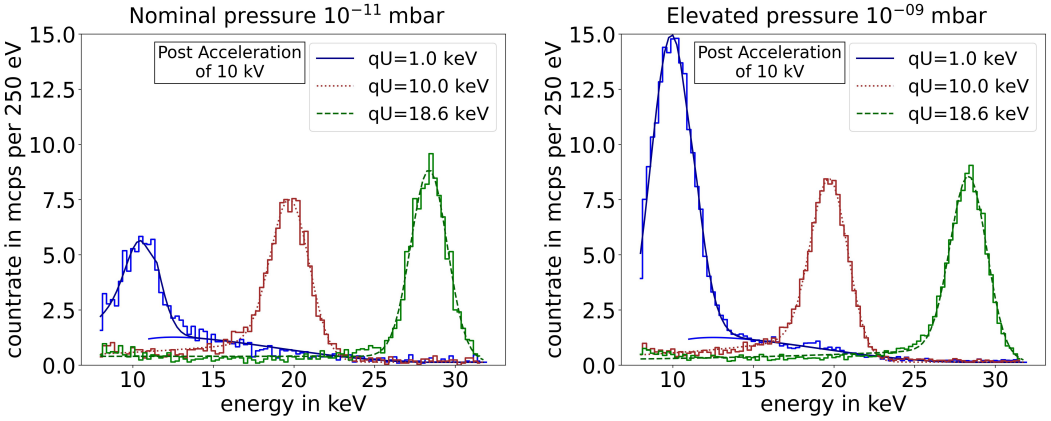

Figure 5.3.: Energy distribution for three different retarding energies of 1.0, 10.0 and 18.6 keV. The PAE was set to +10 kV while pressure was varied with (a) at nominal pressure of $1.8 \cdot 10^{-11}$mbar and (b) at elevated pressure via helium injection of $9.8 \cdot 10^{-10}$mbar.

based on the detector response model of the TRISTAN SDD described in [Sie19]. The gaussian function is used to describe the main energy peak observed, while the exponential step function accounts for the lower energy part of the peak. Using this model the shape of the background distribution can be well reproduced with an energy resolution for the peaks of $FWHM \approx 2.4\,\text{keV}$, which fits well to the FPD resolution. Furthermore, the peak position for low energy background electrons should correspond to the energy of the retarding potential and the PAE $q(U_{\text{ret}} + U_{\text{PAE}})$. This is the case for all measurements except for the measurement at 1 keV and elevated pressure. The deviation for this specific measurement will be further discussed later. All other measurements fit to the expected peak position, but are roughly 300 eV below the exact value of $q(U_{\text{ret}} + U_{\text{PAE}})$. This can be explained by energy losses within the insensitive dead-layer of the detector.

However, there are also some unexpected features visible in the spectra for low retarding energy of 1 keV. Both peaks show a tail towards higher energies, that is not visible in the 10 keV measurement and there is also no indication of it in the 18.6 keV measurement. One explanation can be provided by tritium beta electrons and indeed expanding the fit function for both 1 keV measurements to include a beta decay spectrum

$$R_\beta = R + \theta(E - q(U_{\text{ret}} + U_{\text{PAE}})) \cdot a_\beta \cdot \Gamma(E) \tag{5.2}$$

where θ is the Heaviside function implemented, because all electrons with an energy below the retarding energy are rejected by the high pass filter of the MS, $\Gamma(E)$ is the shape of the β electron energy spectrum and a_β is an arbitrary scaling factor. Including this spectrum matches the observed shape for the background distribution and both fits yield scaling factors a_β that are compatible with each other. Now the question is where do these tritium decay electrons come from, if all source related parts are closed off by valve V4? The answer might be given by the valve itself. During an incident in December 2019[bck] the main spectrometer and consequently also valve V4 have been exposed to a small amount of tritium. By closing the valve electrons from tritium decay can be transmitted onto the detector and explain the tail observed for the measurements at 1 keV.

Comparing the measurements within one pressure setting the peak size tends to decrease for lower retarding energies. This trend is clearly visible for the nominal pressure measurements shown on the left in figure 5.3. It is also visible, although less pronounced when comparing the 18.6 keV and the 10 keV peak of the elevated pressure measurements on the right side of

figure 5.3. However, there is again a deviation for low retarding energies. The peak of the 1 keV measurement at elevated pressure is almost twice as high as other peaks measured at elevated pressures. Its peak position is also shifted by 1 keV and appears at 10 keV instead of the expected $q(U_{\mathrm{ret}} + U_{\mathrm{PAE}}) = 11\,\mathrm{keV}$.

To further investigate the energy tail observed at low retarding energies together with the unexpected rate increase and peak shift for the measurement combination of low retarding energies at elevated pressure conditions another set of background measurements are performed.

5.3. Further investigations at low retarding energies

In order to study the background behavior at low retarding energies another set of background measurements is performed at lower retarding energies. Of particular interest is the combination of low retarding energies together with an elevated main spectrometer pressure. After injecting helium into the MS in static mode an elevated pressure of $1.1 \cdot 10^{-9}\,\mathrm{mbar}$ is achieved. For all results presented in this chapter elevated pressure relates to this pressure. To obtain a reference all measurements are also performed at the nominal KATRIN pressure. The chosen retarding energies together with the measurement time spent at each setpoint can be found in table 5.3. This time 4 hours are spent at each retarding energy , but the retarding energies are again iterated multiple times. All other parameters like the magnetic field and PAE are kept as described in section 5.1.

Table 5.3.: Measurement time in hours spent at each retarding energy

	1.0 keV	2.0 keV	3.0 keV	5.0 keV
Nominal pressure	12 h	12 h	12 h	12 h
Elevated pressure	20 h	16 h	16 h	16 h

The obtained energy distributions for the ROI from 8 to 32 keV and 250 eV binning can be seen in figure 5.4 and 5.5.

For the nominal pressure measurements the expected behavior of the previous measurements can be seen. The distributions show a gaussian peak with a decreasing amplitude towards lower retarding energies. This time the tail of the peaks toward higher energies can be seen in all measurements. Although for the 5 keV measurement the tail is much less pronounced. To characterize the tail each distribution is fit with equation 5.2. The overall shape of the spectra is well reproduced by the fit, however the scale factor of the beta spectrum does not exactly match, especially for the 5 keV measurement.

The same fit is performed for the elevated pressure measurements with the same results. The shape is matched very well, while the scale factor is slightly different for higher retarding energies. However, at elevated pressure the peak height increases toward lower retarding energies. This result confirms the unexpected rate increase observed for the previous background measurements at 1 keV and elevated pressure. This time there is also a trend visible that the peak height increases sharply for retarding energies below 5 keV.

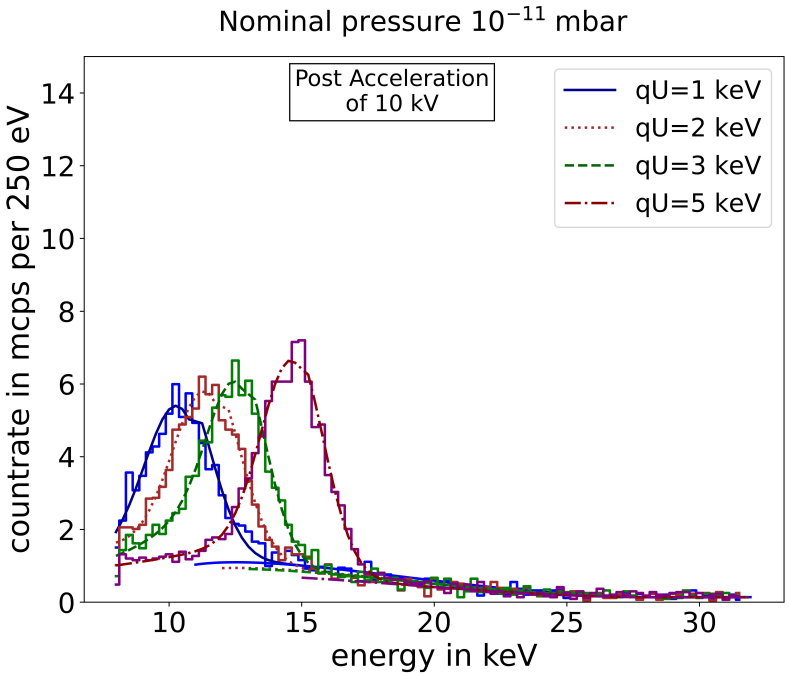

Figure 5.4.: Energy distribution for four different retarding energies of 1.0, 2.0, 3.0 and 5.0 keV with a PAE of +10 kV. All measurements have been performed at nominal pressure of $1.8 \cdot 10^{-11}$mbar.

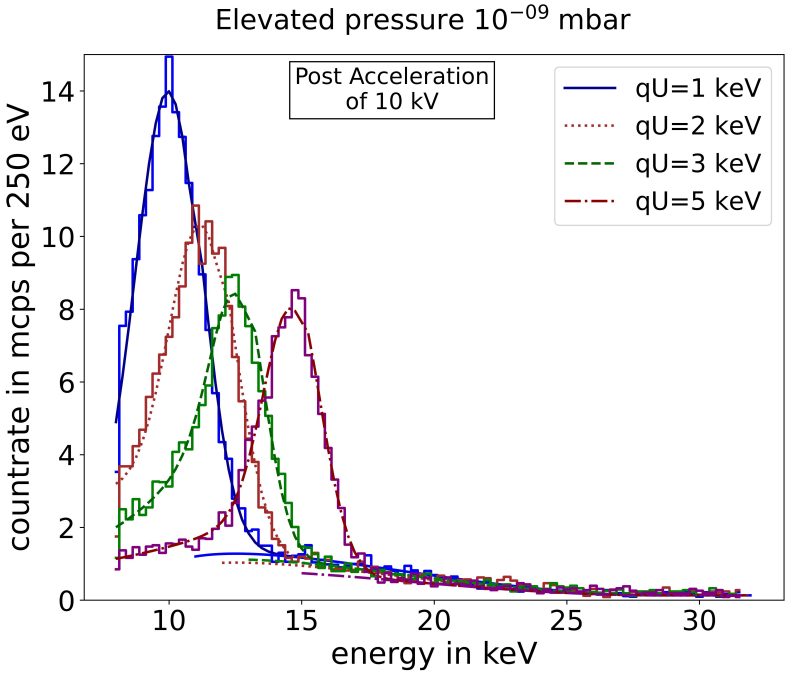

Figure 5.5.: Energy distribution for four different retarding energies of 1.0, 2.0, 3.0 and 5.0 keV with a PAE of +10 kV. All measurements have been performed at elevated pressure of $1.1 \cdot 10^{-9}$mbar.

To further study the cause of this sudden rise, the time distribution between two consecutive events is observed. The distribution of these inter-arrival times is expected to be Poisson distributed if the electrons are uncorrelated.[Blo18][Har15] The inter-arrival time distribution is then given by an exponential function

$$f(t) = a \cdot \exp^{-r \cdot t} \tag{5.3}$$

with the event rate r. The inter-arrival time together with an exponential fit are shown for all measurements at nominal (elevated) pressure in the upper (lower) part of figure 5.6. For the fit all inter-arrival times below 1 second are excluded. The distribution of inter-arrival times show the expected behavior for uncorrelated events. However, for the elevated pressure measurements the distribution below 1 s deviates from that expectation. The insets in figure 5.6 show the distribution below 1 s in blue together with the exponential expectation indicated as dashed black line. Furthermore, the deviation from the expected exponential function increases toward lower retarding energies. So there has to be some production mechanism producing secondary electrons within short time scales and it has to be enhanced for lower retarding energies and at elevated pressure.

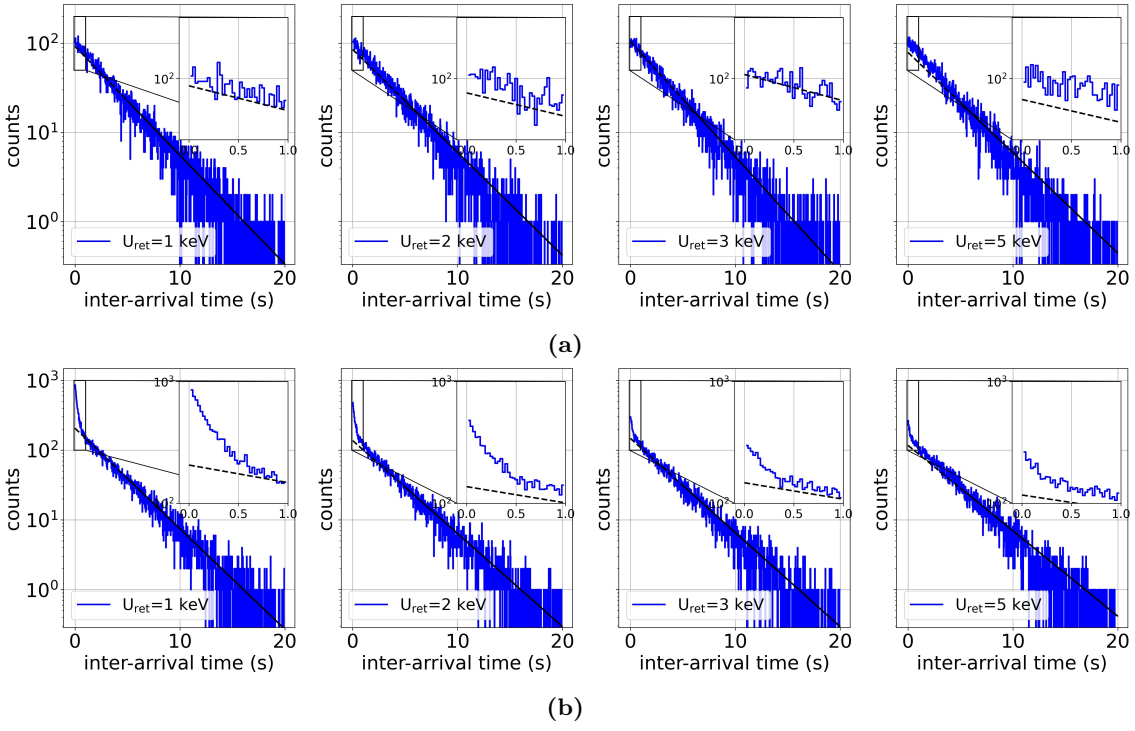

Figure 5.6.: Inter-arrival times for four different retarding energies of 1.0, 2.0, 3.0 and 5.0 keV at (a) nominal pressure of $1.8 \cdot 10^{-11}$mbar and (b) elevated pressure by helium injection to $1.1 \cdot 10^{-9}$mbar. The inter-arrival time distributions of the elevated pressure measurement below 1 s deviate from the expected exponential function indicating correlated events.

To further study the non-poissonian behavior exhibited for short inter-arrival time scales the data set is split into events with an inter-arrival time above and below 1 s. The observed background rate can then also be be split into the contribution given by the Poisson distributed uncorrelated events and the additional rate produced by correlated events that are created by the same production mechanism. Figure 5.7 shows the contribution of the individual parts to the overall countrate measured for each setting. The time refers to the time past since the start of the first measurement. As explained before the retarding potential is changed every four hours and iterates over each retarding energy setting. Countrates are determined by dividing the registered events within the ROI of 8 to 32 keV by the measurement time of each iteration (4 hours). All rates observed for events with inter-arrival times (iaT) greater than 1 second are almost constant around 100 mcps. There is no dependency on the electrostatic settings visible and the results from the different iterations at each setting agree within statistical fluctuations.

The contribution from the correlated events also agree within statistical fluctuations, but exhibit a larger spread between iterations. Additionally, they show a large dependence on the retarding energy setting. Given by the dashed-dotted line is the mean countrate averaged over all iterations at one setting and the shaded are indicates the standard deviation. For the 2 kV measurement the first iteration is excluded from the mean due to its large value. The rate clearly increases toward lower retarding energies in a non-linear way. These results confirm the observations made for the peak heights of the energy distribution and furthermore demonstrate that the observed increase is caused by a retarding energy dependent production mechanism capable of producing several electrons within short time scales.

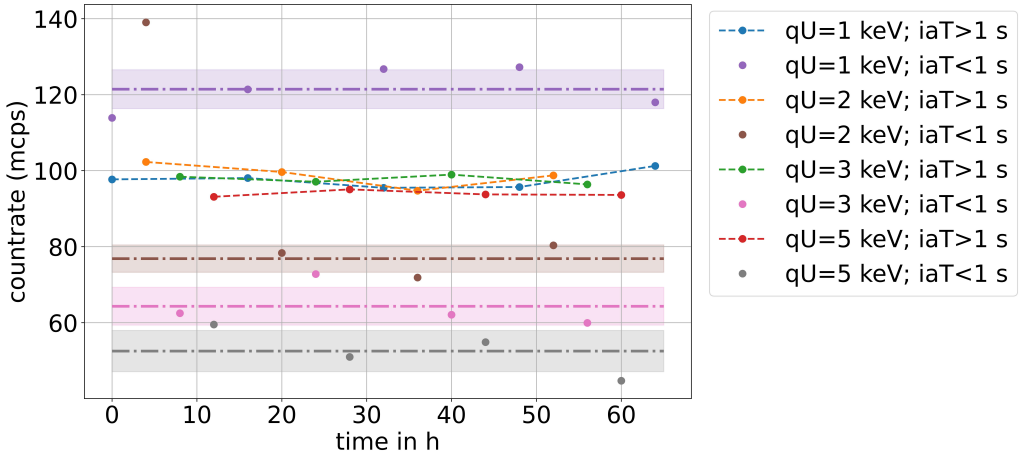

Figure 5.7.: Observed countrates in each measurement iteration at four different retarding energies of 1.0, 2.0, 3.0 and 5.0 keV. Each data set is split into events with an inter-arrival time (iaT) < 1s or ≥ 1s. The mean countrate for events with an inter-arrival time < 1s is given as dashed-dotted line and the shaded areas indicate the standard deviation. For the 2 keV measurement the first iteration is excluded from the mean.

One known background production mechanism that fits this behavior quite well is given by trapped electrons. Charged particles can get trapped inside the main spectrometer due to the magnetic bottle effect. The longitudinal component of their momentum is transformed into the transversal component and vice versa by the magnetic field gradient. Once their polar angle reaches 90° the are reflected. On their path inside the main spectrometer they can ionize residual gas producing low energy secondary electrons. Due to their low energy these secondaries can leave the trap and are registered at the detector. While these particles travel back and forth along the axis of the main spectrometer they also exhibit an azimuthal drift due to radial magnetic field gradients. Therefore, secondary electrons

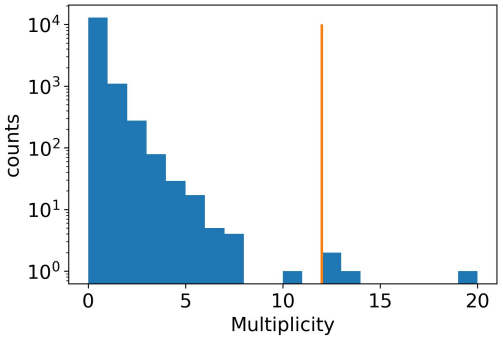

(a) Multiplicity distribution for events recorded within a four hour measurement run at 3.0 keV retarding energy at elevated pressure. The orange vertical line indicates the applied cut. The pixel distribution of all multiplicity events to the right of this line is investigated and show a ring-like structure.

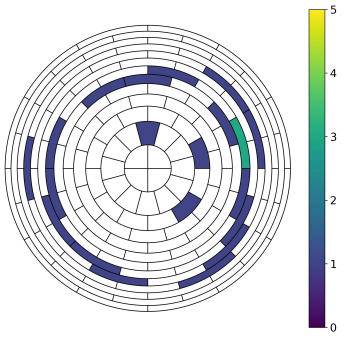

(b) Pixel distribution for a high multiplicity event recorded at a retarding energy of 3.0 keV and elevated pressure of $1.1 \cdot 10^{-9}$mbar. The ring-like structure observed for the secondary electrons hints toward a stored charged particle as production mechanism.

Figure 5.8.

induced by stored electrons create a distinct ring-like pattern on the detector, which can be seen in figure 3.7.

To validate stored electrons as main production mechanism causing the observed rate increase for lower retarding energies below 5 keV at elevated pressure, the pixel distributions are investigated. Only events with inter-arrival times below 1 second are further studied, since the rate increase is mainly related to correlated events. Because several ring-shapes can overlay within the four hour measurement of each iteration, which would result in a constant rate observed over the whole detector, further cuts are applied. For each iteration the multiplicity of events occurring within one second of measurement time is recorded. An exemplary multiplicity distribution is shown in figure 5.8a. Most events have a lower multiplicity, but multiplicities up to 20 can be observed. Looking at the pixel distribution for all events with a multiplicity greater than 12 ring-like structures are observed. An example of such a pixel distribution is given in figure 5.8b.

By splitting the data set into different inter-arrival time contributions it is also possible to investigate the energy distribution of the individual background contributions. Each data set shows the expected gaussian peak shape and is fit with the empirical function including the contribution of β electrons given in equation 5.2 (see figure 5.9). For inter-arrival times greater than 1 second the energy distribution matches the observation at nominal pressure that can been seen in figure 5.4. The spectrum for inter-arrival times below 1 s on the other hand presents two noticeable differences. The peak height observed for these events is not only higher, but also its peak position is shifted. Most events observed in this data set have an energy around 10 keV, which is 1 keV below the expected peak position of $q(U_{\text{ret}} + U_{\text{PAE}}) = 11\,\text{keV}$.

5.4. Possible explanation for shifted energy distribution

In the course of the exploratory background measurements several unexpected features have been observed. All energy distributions show the same gaussian peak shape. However, for low retarding energies below 5.0 keV a tail towards higher energies can be observed. This contribution is independent of the pressure and can be identified with tritium β decay electrons. These electrons are most likely generated at valve V4 that was exposed to tritium during an incident in December 2019[bck].

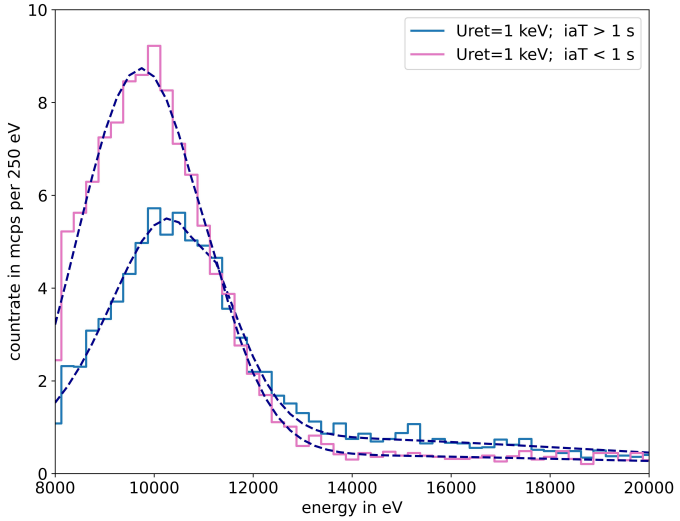

Figure 5.9.: Comparison of energy distribution for a measurement at 1.0 keV retarding energy at an elevated pressure of $1.1 \cdot 10^{-9}$mbar. The events are split by their inter-arrival time (iaT) to demonstrate the effect of secondary electrons created with inter-arrival times below 1 s on the energy distribution. Both spectra are fit with an empirical function given in 5.2. The peak for inter-arrival times above 1 s is at the expected position $q(U_{\mathrm{ret}}+U_{\mathrm{PAE}})$, while the energy peak of the secondaries is shifted down by 1 keV with respect to the expectation.

The peak position is expected to be around the energy of the PAE and retarding energy applied to the main spectrometer, because most background electrons are produced in the lower eV energy range. Furthermore, the peak width should agree with the energy resolution of the detector of $\mathcal{O}$(keV). An energy resolution of approximately 2.4 keV is determined for all peaks fitting well to the FPD energy resolution. The peak position for all retarding energies above 5 keV and/or a pressure of $1.8 \cdot 10^{-11}$mbar agrees well with the expectation. The observed shift towards lower energies in the order of $\mathcal{O}$(100eV) can be explained by typical energy losses in the insensitive dead-layer of the detector.

However, for all measurements performed at lower retarding energies (below 5 keV) and an elevated pressure around 10^{-9}mbar the peak height increases drastically with lower retarding energies. At the same time the peak position also shifts further down towards lower energies. Both the rate increase and the shift can be explained by the contribution of secondary electrons produced within short time scales. The observed time of events together with the pixel distribution of high multiplicity events suggest trapped charged particles as main production mechanism of secondary electrons.

One possible primary particle that can be trapped inside the spectrometer is tritium β electrons originating from valve V4. These electrons are produced close to the PS1 magnet with magnetic fields of 3.1 T and propagate towards the detector. On their way there are three points were electrons might be reflected. Figure 5.10 shows the electromagnetic fields for the MS and outlines how tritium β electrons can cause the observed energy shift of secondary electrons. Any electron with a polar angle above $\theta = xxx$ is already rejected by the PS2 magnetic field before entering the main spectrometer. Only electrons with a polar angle below can enter the main spectrometer and are then filtered by the electrostatic potential U_{ret}. Only electrons with an energy above the retarding energy qU_{ret} and a polar angle below $\theta = xxx$ are transmitted past the analyzing plane, but can still be reflected at the pinch magnet with a magnetic field of $B_{\mathrm{max}} = 4.1$T. The increasing magnetic field gradient transforms the longitudinal momentum component into the transversal one thereby increasing the electrons polar angle. Once a polar angle of 90° is reached the propagation

direction of the electron changes at this turnpoint. Due to the polar angle increase the electrons travel a high distance in a cyclotron motion close to the turnpoint. Therefore, the ionization probability is also highest close to the turnpoint. Because of their low polar angles they can reach quite far into the pinch magnet field only possibly being reflected for magnetic fields above $B_{\mathrm{PS1}} = 3.1\,\mathrm{T}$. At this Z-position along the beamline axis the electrostatic potential of the main spectrometer already falls off. So any secondary electrons produced at the turnpoint are not accelerated by the retarding potential. This would result in an energy distribution of secondary electrons as observed in figure 5.9.

Additionally, the amount of β electrons that can pass the analyzing plane might explain the changing impact of secondary electrons on the energy spectra with the retarding energy. Only electrons that are able to overcome the retarding energy generate secondary electrons that can reach the detector. Furthermore, the amount of secondary electrons produced via ionization of residual gas scales with the primaries energy. By reducing the retarding energy more β electrons pass the AP and at the same time the amount of electrons with higher excess energies increases which both results in an increase of secondary electrons.

It has to be noted that this scenario is so far only qualitatively investigated and has not yet been validated by any simulations or additional measurements.
At the point of this thesis no conclusive evidence of the origin of the trapped primary could be identified. Identifying the primary particle is important, because one possible generation mechanism is related to tritium beta electrons being trapped. In the presented background measurements trapping of β electrons from the tritium contamination on valve V4 can qualitatively explain the observed peak shift in the energy distribution of secondary electrons. However, if this also holds for β electrons from the source the background rate would scale with the source density and this in turn can lead to background rates exceeding the rate of signal electrons. To assess the possibility of trapped β electrons causing the rate increase further simulations and measurements are needed.

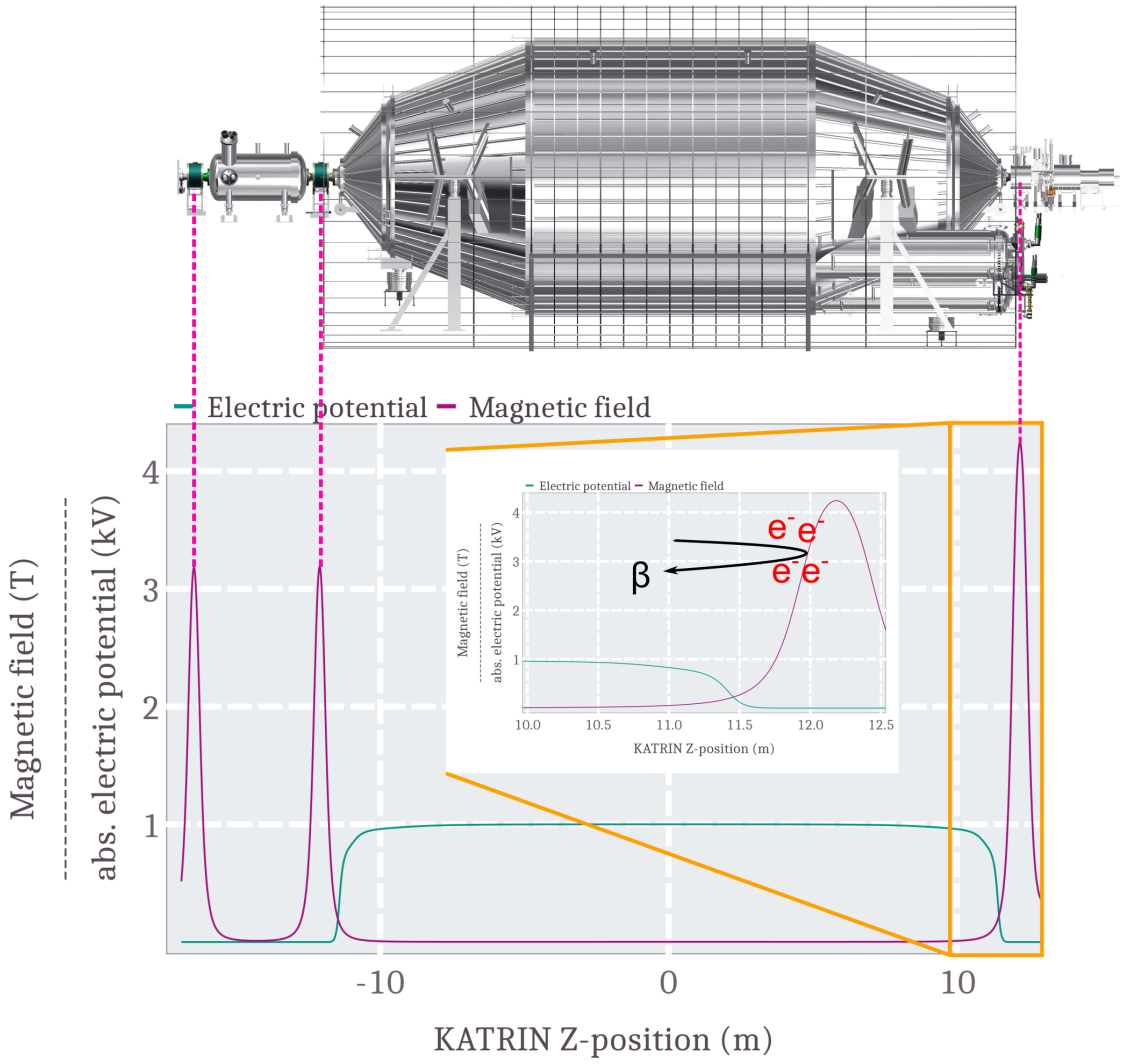

Figure 5.10.: Sketch of secondary electron production mechanism by β electrons produced on valve V4. Only electrons with polar angles above θ = are not already reflected back at the PS2 magnet, but they can be reflected at the higher magnetic field of the pinch magnet. Due to the polar angle change the highest ionization probability is close to the turnpoint of the β electrons. At this point the electric potential of the MS is already falling off and the secondary electrons are only accelerated by the PAE.

6. Conclusion

The KATRIN experiment aims to reach a world leading sensitivity on the neutrino mass of $m_\nu < 0.3\,\mathrm{eV}$ at 90% C.L. by the end of 2026. Afterwards the KATRIN beamline can be used to search for beyond SM physics like keV-sterile neutrinos by performing a high precision measurement of the differential β spectrum. The additional decay branch introduced by keV-sterile neutrinos would lead to a characteristic kink-like structure in the β decay spectrum. By analyzing the position and magnitude of this kink the sterile mass and its mixing amplitude can be inferred.
In order to scan deeper into the spectrum with KATRIN several adjustment to the beamline have to be made. Lower retarding potentials at the high-pass filter of the main spectrometer are needed to cover a larger sterile mass range. This increases the rate of electrons arriving at the detector and also increases the excess energies of these electrons when travelling through the main spectrometer. To assure adiabatic transport through the MS the magnetic field in the analyzing plane has to be increased. Additionally, a new high-resolution TRISTAN SDD capable of handling high rates of 10^8 cps is developed. Due to the modular design of the new detector the high outgassing electronics are no longer fully separated from the UHV spectrometer. This can lead to deteriorated vacuum conditions inside the spectrometer vessel. All of these changes to the KATRIN beamline can lead to changed background levels.

Primary goal of this work is to determine the expected background rates and their energy distribution for keV-sterile neutrino search at KATRIN. Therefore, vacuum simulations of the SDS section are performed to assess the prevailing vacuum conditions in the MS with the integrated TRISTAN modules. It is shown that these simulations can accurately reproduce the current vacuum conditions of the KATRIN setup. The geometry is then extended to include the TRISTAN modules and all planned improvements on the vacuum system of the detector side. This allows predictions on the vacuum conditions of the main spectrometer. The accuracy of these predictions highly depends on the accuracy of key input parameters like the detector outgassing and exact pumping speeds. There have been measurements to determine the outgassing rate of detector parts, however they only provide vague information on the gas composition that is desorbed from the detector. Furthermore, pumping speeds have to be extrapolated for some gases, introducing additional uncertainties to the simulation. Nonetheless, the simulations already provide an estimate on the vacuum compatibility of the TRISTAN detector. Once the input parameters are refined the obtained simulation results can be further improved.

Additionally, a set of exploratory background measurements is performed with an increased magnetic field of $17.6 \cdot 10^{-4}\,\mathrm{T}$ in the AP and different pressures. First, all measurements are performed at the nominal KATRIN pressure in the order of 10^{-11}mbar and then at an elevated pressure in the order of 10^{-9}mbar. Also different retarding energies are cycled over. For all background measurements the energy distribution in the ROI from 8 keV to 32 keV is studied. These measurements revealed a tritium contamination on valve V4. Furthermore, an unexpected background rate increase for lower retarding energies at elevated pressure

is observed. This triggered further investigations of the time distribution of background events, which indicate trapped charged particles as main cause of the observed rate increase. No evidence for any primary charged particle could be identified during this thesis, however a compelling candidate is provided by tritium β electrons. It is discussed how β electrons originating from valve V4 can qualitatively explain all observed features in the background measurements.

Appendix

A. Simulation settings

In the following tables with the exact sticking and their corresponding pumping values for the nominal pumping simulation can be found. The position of each facet selection is shown in figure **??**.

Facet selection	Sticking for gas type H_2	CH_4	H_2O	N_2	CO_2
MS_to_preSpec	0.0069	0.0069	0.0069	0.0069	0.0069
NEG2	0.0261	0.0	0.0261	0.0261	0.0261
NEG3	0.0261	0.0	0.0261	0.0261	0.0261
activeTMPs_PP	0.081	0.301	0.314	0.362	0.411
cryo1	0.167	0.339	0.915	0.408	0.463
getter_detectorSide	0.283	0.0	0.458	0.245	0.286
TMP_detectorSide	0.081	0.304	0.317	0.365	0.415

Table A.1.: Gas dependent sticking factor for each pump in the simulation for the *nominal pumping* setting

Facet selection	Pumping speed in $\frac{L}{s}$ for gas type H_2	CH_4	H_2O	N_2	CO_2
MS_to_preSpec	594	210	198	159	127
NEG2	345	0	115	92	74
NEG3	345	0	115	92	74
activeTMPs_PP	1750	2311	2272	2100	1902
cryo1	2300	1651	4200	1500	1359
getter_detectorSide	3900	0	2100	900	840
TMP_detectorSide	1750	2311	2272	2100	1902

Table A.2.: Gas dependent pumping speed for each pump in the simulation for the *nominal pumping* setting.

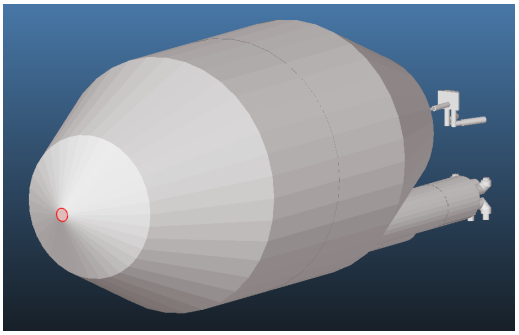

(a) MS_to_preSpec

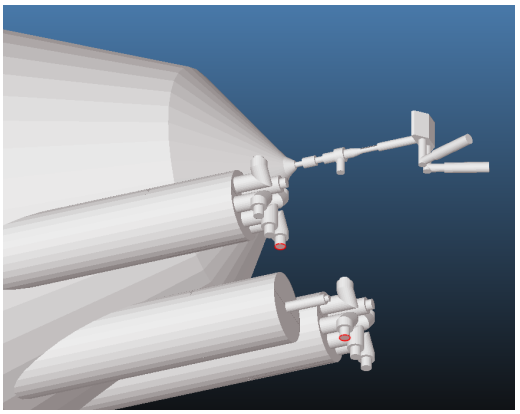

(b) activeTMPs_PP

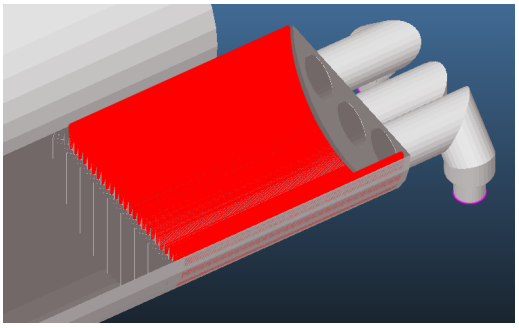

(c) NEG2 cross section. Getter strips are position along the entire circumference of the PP (NEG3 analogous)

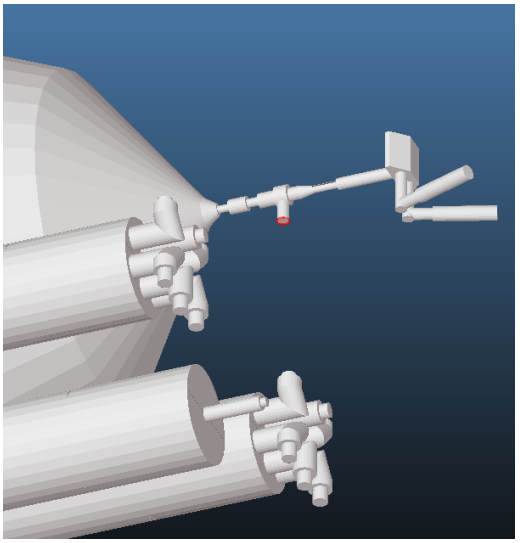

(d) cryo1

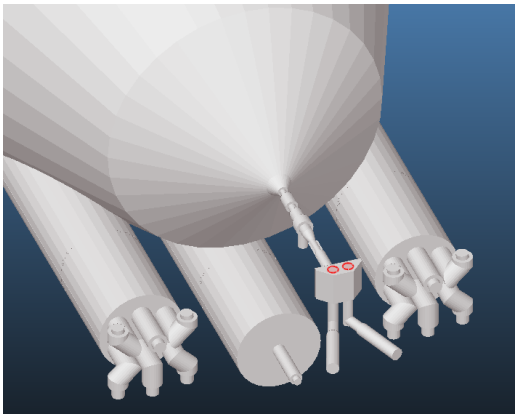

(e) getter_detectorSide

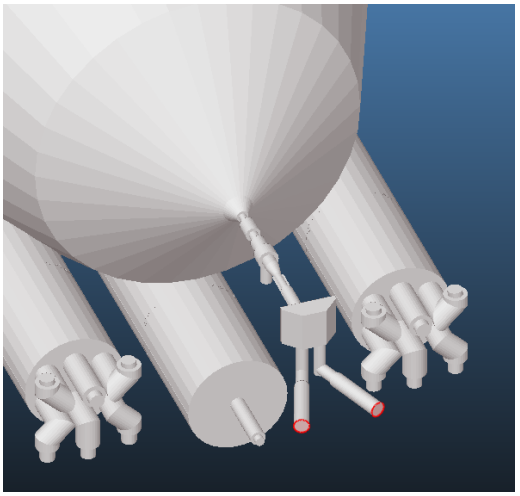

(f) TMP_detectorSide

Figure A.1.: Position of the pumping facets for each facet selection. Facets corresponding to the facet selection are highlighted in red. Pumping speeds or rather sticking factors are set on each facet of a given facet selection.

List of Figures

List of Tables

Bibliography

[A+01] Ahmad, Q. R. *et al.*: *Measurement of the rate of ν_e+d $\rightarrow$ p+p+e^- interactions produced by ^{8}B solar neutrinos at the Sudbury Neutrino Observatory.* Phys. Rev. Lett., 87:071301, 2001.

[A+05] Angrik, J. *et al.*: *KATRIN design report 2004.* Februar 2005.

[A+11] Aseev, V. N. *et al.*: *An upper limit on electron antineutrino mass from Troitsk experiment.* Phys. Rev. D, 84:112003, 2011.

[A+12] Aad, Georges *et al.*: *Observation of a new particle in the search for the Standard Model Higgs boson with the ATLAS detector at the LHC.* Phys. Lett. B, 716:1–29, 2012.

[A+15] Amsbaugh, J. F. *et al.*: *Focal-plane detector system for the KATRIN experiment.* Nucl. Instrum. Meth. A, 778:40–60, 2015.

[A+16] Arenz, M. *et al.*: *Commissioning of the vacuum system of the KATRIN Main Spectrometer.* JINST, 11(04):P04011, 2016.

[A+19a] Aker, M. *et al.*: *Improved Upper Limit on the Neutrino Mass from a Direct Kinematic Method by KATRIN.* Phys. Rev. Lett., 123(22):221802, 2019.

[A+19b] Altenmüller, K. *et al.*: *Gamma-induced background in the KATRIN main spectrometer.* Eur. Phys. J. C, 79(9):807, 2019.

[A+20a] Agostini, M. *et al.*: *Final Results of GERDA on the Search for Neutrinoless Double-β Decay.* Phys. Rev. Lett., 125(25):252502, 2020.

[A+20b] Aker, M. *et al.*: *Suppression of Penning discharges between the KATRIN spectrometers.* Eur. Phys. J. C, 80(9):821, 2020.

[A+21a] Aker, M. *et al.*: *The design, construction, and commissioning of the KATRIN experiment.* JINST, 16(08):T08015, 2021.

[A+21b] Arnquist, I. J. *et al.*: *Search for double-β decay of ^{76}Ge to excited states of ^{76}Se with the MAJORANA DEMONSTRATOR.* Phys. Rev. C, 103(1):015501, 2021.

[A+22a] Acero, M. A. *et al.*: *Improved measurement of neutrino oscillation parameters by the NOvA experiment.* Phys. Rev. D, 106(3):032004, 2022.

[A+22b] Adams, D. Q. *et al.*: *New Direct Limit on Neutrinoless Double Beta Decay Half-Life of Te128 with CUORE.* Phys. Rev. Lett., 129(22):222501, 2022.

[A+22c] Adams, D. Q. *et al.*: *Search for Majorana neutrinos exploiting millikelvin cryogenics with CUORE.* Nature, 604(7904):53–58, 2022.

[A+22d] Aker, M. *et al.*: *Direct neutrino-mass measurement with sub-electronvolt sensitivity.* Nature Phys., 18(2):160–166, 2022.

[A+23a] Abbasi, R. *et al.*: *Measurement of atmospheric neutrino mixing with improved IceCube DeepCore calibration and data processing.* Phys. Rev. D, 108(1):012014, 2023.

[A+23b] Abe, K. *et al.*: *Updated T2K measurements of muon neutrino and antineutrino disappearance using 3.6×1021 protons on target.* Phys. Rev. D, 108(7):072011, 2023.

[A+23c] An, F. P. *et al.*: *Precision Measurement of Reactor Antineutrino Oscillation at Kilometer-Scale Baselines by Daya Bay.* Phys. Rev. Lett., 130(16):161802, 2023.

[A+24] Aker, M. *et al.*: *Direct neutrino-mass measurement based on 259 days of KATRIN data.* Juni 2024.

[AA+18] Aguilar-Arevalo, A. A. *et al.*: *Significant Excess of ElectronLike Events in the MiniBooNE Short-Baseline Neutrino Experiment.* Phys. Rev. Lett., 121(22):221801, 2018.

[AAB+01] Aguilar, A., L. B. Auerbach, R. L. Burman *et al.*: *Evidence for neutrino oscillations from the observation of $\overline{\nu}_e$ appearance in a $\overline{\nu}_\mu$ beam.* Phys. Rev. D, 64:112007, Nov 2001. https://link.aps.org/doi/10.1103/PhysRevD.64.112007.

[Ady] Ady, Marton: *MolFlow+ website.* https://molflow.web.cern.ch/. Last accessed: 13.07.2024.

[AK19] Ady, Marton und Roberto Kersevan: *Recent Developements of Monte-Carlo codes MolFlow+ and Synrad+*, 2019.

[AKL16] Ady, Marton, Roberto Kersevan und Rivkin Leonid: *Monte Carlo simulations of ultra high vacuum and synchrotron radiation for particle accelerators*, 2016. PhD thesis.

[BBS68] Bahcall, John N., Neta A. Bahcall und G. Shaviv: *Present status of the theoretical predictions for the Cl-36 solar neutrino experiment.* Phys. Rev. Lett., 20:1209–1212, 1968.

[bck] *Internal Report.* https://iap-katrin-wiki.iap.kit.edu/katrin/index.php/KNM_Backgrounds#Background_after_Dec._9th,_2019. Last Accessed: 23.07.2024.

[BDL+19] Boyarsky, A., M. Drewes, T. Lasserre, S. Mertens und O. Ruchayskiy: *Sterile neutrino Dark Matter.* Prog. Part. Nucl. Phys., 104:1–45, 2019.

[Bec96] Becquerel, Henri: *Sur les propriétés différentes des radiations invisibles émises par les sels d'uranium, et du rayonnement de la paroi anticathodique d'un tube de Crookes.* Comptes Rendus de l'Académie des sciences, Seiten 762–767, 1896.

[Bel04] Bellerive, Alain: *Review of solar neutrino experiments.* Int. J. Mod. Phys. A, 19:1167–1179, 2004.

[BES80] Bond, J. R., G. Efstathiou und J. Silk: *Massive Neutrinos and the Large-Scale Structure of the Universe.* Phys. Rev. Lett., 45:1980–1984, Dec 1980. https://link.aps.org/doi/10.1103/PhysRevLett.45.1980.

[Blo18] Block, Fabian: *Characterisation of the Background in the KATRIN Experiment.* https://www.katrin.kit.edu/publikationen/mth_fblock.pdf, 2018.

[BMT04] Barger, V., Danny Marfatia und Adam Tregre: *Neutrino mass limits from SDSS, 2dFGRS and WMAP*. Physics Letters B, 595(1–4):55–59, August 2004, ISSN 0370-2693. http://dx.doi.org/10.1016/j.physletb.2004.06.049.

[BRS09] Boyarsky, Alexey, Oleg Ruchayskiy und Mikhail Shaposhnikov: *The Role of sterile neutrinos in cosmology and astrophysics*. Ann. Rev. Nucl. Part. Sci., 59:191–214, 2009.

[BSB05] Bahcall, John N., Aldo M. Serenelli und Sarbani Basu: *New solar opacities, abundances, helioseismology, and neutrino fluxes*. Astrophys. J. Lett., 621:L85–L88, 2005.

[BU88] Bahcall, John N. und Roger K. Ulrich: *Solar Models, Neutrino Experiments and Helioseismology*. Rev. Mod. Phys., 60:297–372, 1988.

[C+12] Chatrchyan, Serguei *et al.*: *Observation of a New Boson at a Mass of 125 GeV with the CMS Experiment at the LHC*. Phys. Lett. B, 716:30–61, 2012.

[Cal24] Calgaro, S.: *The LEGEND experiment for the search for the Majorana neutrino*. Nuovo Cim. C, 47(3):69, 2024.

[CER99] Chu, S.Y.F, L.P. Ekström und Firestone R.B.: *WWW Table of Radioactive Isotopes*, 1999. last accessed: 12.07.2024.

[CGR06] Choi, JH, J. Guest und G. Raithel: *Magnetic trapping of strongly-magnetized Rydberg atoms*. European Physics Journal D, 40:19–26, April 2006.

[Cha14] Chadwick, J.: *The intensity distribution in the magnetic spectrum of beta particles from radium (B + C)*. Verh. Phys. Gesell., 16:383–391, 1914.

[CR+56] Cowan, C. L., F. Reines *et al.*: *Detection of the free neutrino: A Confirmation*. Science, 124, 1956.

[cry] *Marathon CP-8 data sheet*. https://fuzzy.ipe.kit.edu/bscw/bscw.cgi/719067?op=preview&back_url=467819. Last Accessed: 18.07.2024.

[CS10] Canetti, Laurent und Mikhail Shaposhnikov: *Baryon asymmetry of the Universe in the nuMSM*. Journal of Cosmology and Astroparticle Physics, 2010(09):001, sep 2010. https://dx.doi.org/10.1088/1475-7516/2010/09/001.

[Cur03] Curie, Marie: *Untersuchungen über die radioaktiven Substanzen*, Band 1. F. Vieweg und Sohn, Braunschweig, 1903.

[Des24] Descher, Martin: *Differential spectrum modeling and sensitivity for keV sterile neutrino search at KATRIN*, 2024.

[DGGK17] Drewes, Marco, Bjorn Garbrecht, Dario Gueter und Juraj Klaric: *Testing the low scale seesaw and leptogenesis*. JHEP, 08:018, 2017.

[DHH68] Davis, Jr., Raymond, Don S. Harmer und Kenneth C. Hoffman: *Search for neutrinos from the sun*. Phys. Rev. Lett., 20:1205–1209, 1968.

[DHMW13] Drexlin, G., V. Hannen, S. Mertens und C. Weinheimer: *Current direct neutrino mass experiments*. Adv. High Energy Phys., 2013:293986, 2013.

[Die11] Diehl, Christoph: *First mass measurements with the MPIK/UW-PTMS*. Januar 2011.

[DLBM07] Day, Ch., X. Luo, A. Bonucci und P. Manini: *Determination of the sticking probability of a Zr–V–Fe nonevaporable getter strip*. J. Vac. Sci. Technol. A, 25(4):824–830, 2007.

[DON01] DONUT Collaboration: *Oberservation of tau neutrino interactions.* Phys. Lett. B, 504(3), 2001.

[DPR19] Dolinski, Michelle J., Alan W. P. Poon und Werner Rodejohann: *Neutrinoless Double-Beta Decay: Status and Prospects.* Ann. Rev. Nucl. Part. Sci., 69:219–251, 2019.

[DR16] D'Onofrio, Michela und Kari Rummukainen: *Standard model cross-over on the lattice.* Phys. Rev. D, 93(2):025003, 2016.

[DW94] Dodelson, Scott und Lawrence M. Widrow: *Sterile-neutrinos as dark matter.* Phys. Rev. Lett., 72:17–20, 1994.

[E+18] Erhard, M. *et al.*: *Technical design and commissioning of the KATRIN large-volume air coil system.* JINST, 13(02):P02003, 2018.

[F+98] Fukuda, Y. *et al.*: *Evidence for oscillation of atmospheric neutrinos.* Phys. Rev. Lett., 81:1562–1567, 1998.

[Fra23] Fraenkle, Florian: *Update on the background*, 2023.

[GDL+13] Glück, Ferenc, Guido Drexlin, Benjamin Leiber, Susanne Mertens, Alexander Osipowicz, Jan Reich und Nancy Wandkowsky: *Electromagnetic design of the large-volume air coil system of the KATRIN experiment.* New J. Phys., 15:083025, 2013.

[GGS58] Goldhaber, M., L. Grodzins und A. W. Sunyar: *Helicity of Neutrinos.* Phys. Rev., 109:1015–1017, Feb 1958. `https://link.aps.org/doi/10.1103/PhysRev.109.1015`.

[GL11] Giunti, Carlo und Marco Laveder: *Statistical significance of the gallium anomaly.* Phys. Rev. C, 83:065504, Jun 2011. `https://link.aps.org/doi/10.1103/PhysRevC.83.065504`.

[Har15] Harms, Fabian: *Characterization and Minimization of Background Processes in the KATRIN Main Spectrometer*, 2015.

[Hil] Hiller, Roman: *Post acceleration electrode.*

[Hin22] Hinz, Dominic: *Background systematics and extensions to the KATRIN background model*, 2022.

[Hub15] Huber, Anton: *Search for keV-Scale Sterile Neutrinos with KATRIN*, 2015.

[Hub21] Huber, Anton: *Analysis of first KATRIN data and searches for keV-scale sterile neutrinos*, 2021.

[K+04] Kraus, C. *et al.*: *Latest results from the Mainz Neutrino Mass Experiment.* Eur. Phys. J. C, 33:S805–S807, 2004.

[K+23] Kharusi, S. Al *et al.*: *Search for two-neutrino double-beta decay of ^{136}Xe to the excited state of ^{136}Ba with the complete EXO-200 dataset*.* Chin. Phys. C, 47(10):103001, 2023.

[KMMS13] Kopp, Joachim, Pedro A. N. Machado, Michele Maltoni und Thomas Schwetz: *Sterile Neutrino Oscillations: The Global Picture.* JHEP, 05:050, 2013.

[Knu09] Knudsen, Martin: *Die Gesetze der Molekularströmung und der inneren Reibungsströmung der Gase durch Röhren.* Annalen der Physik, 333(1):75–130, Januar 1909.

[KSGS19] Kostensalo, Joel, Jouni Suhonen, Carlo Giunti und Praveen C. Srivastava: *The gallium anomaly revisited.* Phys. Lett. B, 795:542–547, 2019.

[Lei14] Leiber, Benjamin: *Investigations of Background Due to Secondary Electron Emission in the KATRIN-Experiment.* Dissertation, KIT, Karlsruhe, 2014.

[Lin15] Linek, Johanna: *Investigation of the muon induced background at the KATRIN main spectrometer.* `https://www.katrin.kit.edu/publikationen/mth-Linek.pdf`, 2015.

[LP06] Lesgourgues, Julien und Sergio Pastor: *Massive neutrinos and cosmology.* Physics Reports, 429(6):307–379, 2006, ISSN 0370-1573. `https://www.sciencedirect.com/science/article/pii/S0370157306001359`.

[LP12] Lesgourgues, Julien und Sergio Pastor: *Neutrino mass from Cosmology.* Adv. High Energy Phys., 2012:608515, 2012.

[LSS+62] Lederman, L. M., M. Schwartz, J. Steinberger *et al.*: *Observation of High-Energy Neutrino Reactions and the Existence of Two Kinds of Neutrinos.* Phys. Rev. Lett., 9, Jul 1962. `https://link.aps.org/doi/10.1103/PhysRevLett.9.36`.

[M+13] Mertens, S. *et al.*: *Background due to stored electrons following nuclear decays in the KATRIN spectrometers and its impact on the neutrino mass sensitivity.* Astropart. Phys., 41:52–62, 2013.

[M+19] Mertens, Susanne *et al.*: *A novel detector system for KATRIN to search for keV-scale sterile neutrinos.* J. Phys. G, 46(6):065203, 2019.

[Mal07] Malyshev, Oleg B.: *Characterisation of a turbo-molecular pumps by a minimum of parameters.* Vacuum, 81(6):752–758, 2007.

[Mer12] Mertens, Susanne: *Study of Background Processes in the Electrostatic Spectrometers of the KATRIN Experiment*, 2012.

[N+24] Navas, S. *et al.*: *The Review Of Particle Physics.* Phys. Rev. D, 110(3):030001, 2024.

[NEG] *CapaciTorr Z 3500 data sheet.* `https://www.ferrovac.com/?tool=SysFileFetch&file=CAPACITorrZ3500.pdf`. Last Accessed: 18.07.2024.

[P+75] Perl, M. L. *et al.*: *Evidence for Anomalous Lepton Production in $e^+ - e^-$ Annihilation.* Phys. Rev. Lett., 35, 1975. `https://link.aps.org/doi/10.1103/PhysRevLett.35.1489`.

[Pau30] Pauli, W.: *Offener Brief an die Gruppe der Radioaktiven bei der Gauvereins-Tagung zu Tübingen.* In: Meyenn, K.v. (Herausgeber): *Scientific Correspondence with Bohr, Einstein, Heisenberg a.o. Volume II: 1930–1939.* Springer-Verlag, Berlin a.o., 1930.

[Peh24] Pehov, Alexey: *Probing the neutrino mass scale with the KATRIN experiment.* 2024. `https://indico.cern.ch/event/1199289/contributions/5447195/attachments/2705052/4695809/Lokhov_KATRIN_TAUP2023_short.pdf`.

[Pfe13] Pfeiffer vacuum GmbH: *The Vacuum Technology Book; Volume 2.* Pfeiffer Vacuum GmbH, 2013.

[Pon67] Pontecorvo, B.: *Neutrino Experiments and the Problem of Conservation of Leptonic Charge.* Zh. Eksp. Teor. Fiz., 53:1717–1725, 1967.

[Pur22] Puritscher, Moritz: *Determination of the TRISTAN phase-1 detector model gas dynamic conductance*, 2022.

[PW82] Pal, Palash B. und Lincoln Wolfenstein: *Radiative Decays of Massive Neutrinos*. Phys. Rev. D, 25:766, 1982.

[RS13] Ravikumar, P. und R.K. Somashekar: *ESTIMATES OF THE DOSE OF RADON AND ITS PROGENY INHALED INSIDE BUILDINGS*. European Journal of Environmental Science, 3:88–95, Januar 2013.

[Sch14] Schwarz, Johannes Simon: *The Detector System of the KATRIN Experiment - Implementation and First Measurements with the Spectrometer*, 2014.

[SF99] Shi, Xiang Dong und George M. Fuller: *A New dark matter candidate: Nonthermal sterile neutrinos*. Phys. Rev. Lett., 82:2832–2835, 1999.

[Sha07] Shaposhnikov, Mikhail: *A possible symmetry of the nuMSM*. Nuclear Physics B, 763(1):49–59, 2007, ISSN 0550-3213. https://www.sciencedirect.com/science/article/pii/S0550321306008960.

[Sha21] Shaastra. https://shaastramag.iitm.ac.in/first-principles/standard-model-particle-physics, 2021. last accessed: 15.07.2024.

[Sie19] Siegmann, Daniel: *Investigation of the Detector Response to Electrons of the TRISTAN Prototype Detectors*, 2019.

[Suz91] Suzuki, A.: *Kamiokande solar neutrino experiment and solar neutrino problem*. In: *International Workshop on Electroweak Physics: Beyond the Standard Model*, Dezember 1991.

[TMP] *Turbovac MAG W 2200 iP data sheet*. https://www.leyboldproducts.de/media/pdf/16/1d/f4/_POD_CP_040_DE_Hochvakuumpumpen_LV_2021.pdf. Last Accessed: 18.07.2024.

[TRI21] TRISTAN group: *Conceptual Design Report for KATRIN with TRISTAN detectors*. https://www.katrin.kit.edu/downloads/TRISTAN__Technical_Design_Report%20(10).pdf, 2021.

[Tro19] Trost, Nikolaus Rainer Maria: *Modeling and measurement of Rydberg-State mediated Background at the KATRIN Main Spectrometer*. Dissertation, Karlsruhe U., 2019.

[Ull20] Ullmer, Lars: *Investigations on the vacuum compatibility of the first TRISTAN detector module*, 2020.

[Vol02] Volkas, R.R.: *Introduction to sterile neutrinos*. Progress in Particle and Nuclear Physics, 48(1):161–174, 2002, ISSN 0146-6410. https://www.sciencedirect.com/science/article/pii/S0146641002001229.

[WAH+57] Wu, C. S., E. Ambler, R. W. Hayward, D. D. Hoppes und R. P. Hudson: *Experimental Test of Parity Conservation in Beta Decay*. Phys. Rev., 105:1413–1415, Feb 1957. https://link.aps.org/doi/10.1103/PhysRev.105.1413.

[WLP12] Watson, Casey R., Zhi Yuan Li und Nicholas K. Polley: *Constraining Sterile Neutrino Warm Dark Matter with Chandra Observations of the Andromeda Galaxy*. JCAP, 03:018, 2012.

[Wol] Wolf, Joachim. Personal correspondance.